Properties of Materials

Editor
İlyas UYGUR

BİDGE

BIDGE Publications

Properties of Materials

Editor: Prof. Dr. İlyas UYGUR

ISBN: 978-625-6707-34-4

Page Layout: Gözde YÜCEL

1st Edition:

Publication Date: 25.12.2023

BIDGE Publications,

Certificate No: 71374

www.bidgeyayinlari.com.tr - bidgeyayinlari@gmail.com

Krc Bilişim Ticaret ve Organizasyon Ltd. Şti.
Güzeltepe Mahallesi Abidin Daver Sokak Sefer Apartmanı No: 7/9 Çankaya / Ankara

PREFACE

Properties of materials comprise a vast subject and play a dominant role when choosing specific materials from the thousands available. However, these properties can be classified into three main sections. Firstly, mechanical properties; such as tensile strength, bending strength, shear strength, wear resistance, fatigue strength, and creep response, among others. Secondly, physical properties including chemical composition, melting temperature, density, heat and electrical conductivity, optical properties, and corrosion resistance, etc. Lastly, technological properties such as castability, formability, malleability, machinability, and weldability, etc. Each of these properties is crucial and significantly affects the durability, quality, and performance of materials in products.

In this book, one major property is chosen in each class and thoroughly discussed. Fatigue, corrosion, 3D printers, and fuel cells receive particular attention in this regard. I believe that this book will be significantly beneficial for undergraduate and graduate students, as well as curious researchers in various industries.

Editor

Prof.Dr. İlyas UYGUR

Contents

CHAPTER I

Effects on the Corrosion Properties of Mg-Doped and Homogenization process for Al-Fe Alloys

Hayrettin AHLATÇI[1]
Yunus TÜREN[2]
Fatma MEYDANERİ TEZEL[3]

Introduction

Aluminum alloys have widespread application in the electric power industry as a result of their high strength/density and good formability, excellent electrical conductivity (Sauvage et al., 2015; Karabay, 2006; Yuan& Liang, 2011; Ji et al., 2016; Hosseinifar&

[1]Prof. Dr., Karabük University, Faculty of Engineering, Department of Metallurgy and Materials Engineering, 78050, Karabük, Türkiye. E-mail: hahlatci@karabuk.edu.tr,ORCID: 0000-0002-6766-4974
[2]Associate Prof. Dr., Necmettin Erbakan University, Faculty of Engineering, Department of Mechanical Engineering, 42090, Konya, Türkiye. E-mail: yunus.turen@erbakan.edu.tr, ORCID:0000-0001-8755-1865
[3]Prof. Dr., Karabük University, Faculty of Engineering, Department of Metallurgy and Materials Engineering, 78050, Karabük, Türkiye.E-mail: fatmameydaneri@karabuk.edu.tr, ORCID: 0000-0003-1546-875X

Malakhov, 2008; Valiev et al., 2014). Al alloys are widely used in applications in the automotive industry, especially due to their low density and light weight. Alloying elements are added to Al alloys to suppress grain growth at the examined temperatures, to achieve the desired properties during modification of metallic and intermetallic phases or grain refinement, dispersion strengthening, solid solution hardening, precipitation hardening (Cole& Sherman,1995; Burger et al.,1995; Jinta et al.,2000). Addition of Mg to Al alloys improves properties such as dispersion strength, strengthening and hardening with solid solution of Al alloys, corrosion resistance, low-cycle fatigue resistance and weldability without significantly reducing ductility (Toros et al., 2008; Lloyd&Court, 2003).

Al-Mg alloys have no second phase particles at optimum temperatures for superplasticity, i.e., they form minimal voids during plastic yielding between 450 °C and 500 °C. It has been shown by many researchers that fine-grained microstructure can be obtained from Al-Mg alloys by adding appropriate third elements such as Cr, Zr or Mn, usually less than 1 wt.% (Taleff et al.,1996; Sheppard et al.,1983; McNelley&Hales,1995). Al-Mg alloy is widely used in industry due to its low density, high ductility, castability, weldability and high corrosion resistance (Cho et al., 2020; Engler et al. ,2017; Mostafaei, 2019; Che et al., 2017). More Al alloys that are economical and environmentally friendly can now be recycled. However, iron is also seen in this alloy, as are the elements and impurities in it (Cao & Campbell, 2004; Que et al., 2018; Khalifa et al., 2003).

Researchs on the effects of Mg as a solute in Al-Mg alloys have focused on its growth restriction effect. Some studies have shown that the effect of Mg on the grain confinement of α-Al is quite complex to be taken into account with a single parameter (Birol, 2012; Que e al., 2021). Iron is a damaging element due to its low solubility in α-Al (<0.04%). The presence of iron enables the formation of iron-rich intermetallic compounds (such as $Al_{13}Fe_4$, β-Al_5FeSi, α-Al_8Fe_2Si). These iron-rich intermetallics normally have

low symmetry. For example, $Al_{13}Fe_4$ and β-Al_5FeSi are monoclinic, α-Al_8Fe_2Si is hexagonal, but tends to form acicular-like during solidification. This Al alloys, grain refinement of these FIMCs is very important to strengthen the mechanical properties. Therefore, deformation (Shabestari&Ghanbari, 2010), ultrasonic treatment (Zhang et al., 2013), structure modification (Wang et al., 2016; Suárez-Peña& Asensio-Lozano, 2006; Samuel& Samuel, 1997), grain refiner addition (Smith et al., 2013; Lui et al., 2019; Hassani et al., 2012) are used for refining FIMCs. The mechanism of grain refinement by grafting is understood as the provision of alloying elements for grain confinement and potential particles for heterogeneous nucleation (Fan et al., 2015; Que et al., 2017). The chemical method is an effective and economical way for grain refinement of Al alloys during the solidification process. Recent research (Que et al., 2017) shows that the nucleation undercooling of FIMCs is significantly higher than that of pure metals such as Al and Mg.

As seen in the literature, additive metals to aluminum and its alloys not only improve the existing properties of the alloy, but also present some disadvantages. In order to minimize these disadvantages, such alloys can be made more suitable by applying heat treatments. In this study, corrosion behavior was investigated by applying Mg(x=1, 2, 3 wt.%) addition to the Al-Fe alloy and homogenization annealing at 500 °C for 5 hours.

Materials and methods

Al shots, coarse pure Fe particles and pure Mg plates were used for casting of the examined Al-21.1Fe and Al-yFe-xMg (y = 20.1, 19.1, 18.1 and x = 1, 2, 3 wt.%) alloys in this study. From the phase diagrams, the composition of the Al-Fe alloy was determined and the mass ratios of the elements were calculated and the casting stage was started. Casting of the alloys was carried out in an induction casting furnace. First of all, pure Al was melted at 750 °C and Fe particles were added into the liquid melt at approximately 850 °C. The Fe particles were dissolved in the molten Al and turned into a

homogeneous melt by mixing with a graphite rod for half an hour. When the temperature was gradually reduced and reached 750 °C, the pure Mg (1,2,3 wt.%) was added into the melt and then casting was carried out in metal mold. Solidified samples were prepared as casting samples and samples to be subjected to 5-hour homogenization annealing at 500 °C. In the first stage, the samples were cut, bakelite and polished with 6, 3, 1 micron diamond suspensions, respectively, and after ultrasonic polishing, they were etched with Keller solution (2.5 ml HNO_3+ 1.5 ml HCl + 1.0 ml HF + 95 ml H_2O) and made ready for imaging their surface morphologies.

Detailed surface morphologies and EDS elemental mappings of all Al-Fe and Al-Fe-xMg (x=1, 2, 3 wt.%) casting and homogenization annealed samples were obtained with the CARL ZEISS ULTRA PLUS GEMINI brand FESEM device.

Finally, for all samples, their corrosive behavior was examined by immersion in 3.5% NaCl solution and by performing potentiodynamic corrosion tests with the Gamry brand Potentiostat/Galvanostat/Zero Resistance Ammeter device (Figure 1). Immersion corrosion tests of the examined as-cast and homogenized Al-Fe and Al-Fe-xMg alloys were carried out in 3.5% NaCl solution at specified intervals within 24 hours, by removing the samples from the solution and cleaning them ultrasonically in dilute nitric acid solution, and then their weights were measured by using an electronic balance with a sensitivity of 0.1 mg. Electrochemical corrosion tests of as-cast and homogenized Al-Fe and Al-Fe-xMg alloys in a 250 ml volume of 3.5% NaCl solution were performed with a Gamry model PCI4/300 mA potentiostat/galvanostat corrosion tester with computer-controlled DC105 corrosion analysis using a standard three-electrode cell. Samples were encapsulated in cold-setting resin, leaving a surface area of 0.196 cm^2 exposed to the solution. A copper cable placed behind the resin-coated sample was used for electrical connection. A graphite rod with a diameter of 10 mm and a length of 100 mm was used as the counter electrode, a saturated calomel electrode (SCE) as the reference electrode, and a

classical three-electrode cell with the sample surface as the working electrode. Open circuit potential (OCP) was monitored as a function of time after immersion. For polarization curve measurement, a polarization scan was performed in the range of -0.25 V (vs. open circuit potential, Eoc) to +0.25 V (vs. Eoc) at a scan rate of 1 $mV.s^{-1}$. Three potentiodynamic polarization tests were performed for each parameter and the average of the results was taken.

Figure 1. Gamry brand Potentiostat/Galvanostat/Zero Resistance Ammeter device.

Results and discussion

Surface morphology and EDS mapping analysis

Matrix phase, distribution and shapes of intermetallic phases, grain boundaries and casting defects, etc. microstructural investigations were made and imaged. FESEM images of the casting samples and samples to be subjected to 5-hour homogenization annealing at 500 °C are given in Figure 2. θ-$Al_{13}Fe_4$+α-Al eutectic phase was formed within the white α-Al matrix phase in both Al-21.1 wt.% Fe samples that were cast and homogenized annealed. With this annealing, the structure of the eutectic lamellae in the white α-Al phase increased and became thinner. In addition, the long and

thick-bodied structure is separated by intermetallic θ-$Al_{13}Fe_4$ phase and α-Al phases. That is, the microstructure of the Al-Mg-Fe alloy triggers the formation of maintain Mg-rich Al matrix phases due to the chemical inertness between Mg and Fe and application of homogeneous annealing, since Mg has some solubility in Al (α-Al+Al_3Mg_2, Al_3Mg_2=β-AlMg), a eutectic structure is formed, and the eutectic phase (α-Al+Al_3Mg_2) in the white α-Al matrix phase will become more dominant. With homogenization annealing, the long-thick body intermetallic structure will begin to thin and while turn into a small needle-like structure, medium-sized spherical structures and dendrite arms will continue to grow. Additionally, the EDS mapping of the cast and homogenized samples is given in Figures 3 and 4, respectively.

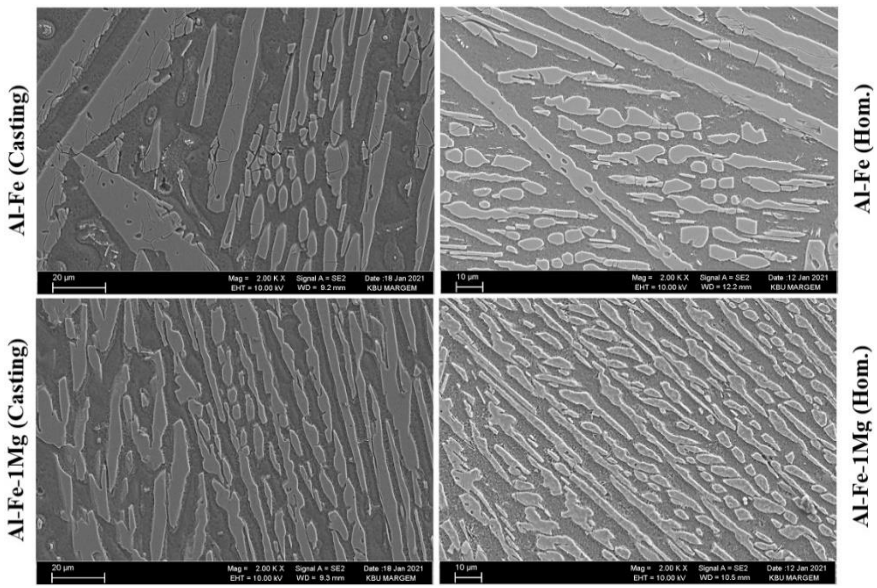

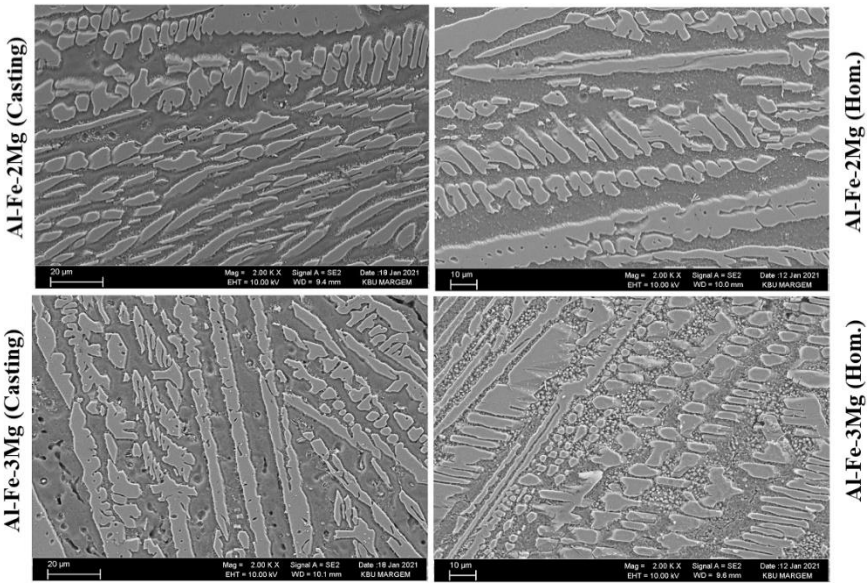

Figure 2. FESEM images of the casting and homogenized samples for Al-Fe ve Al-Fe-xMg (x=1, 2, 3 wt.%).

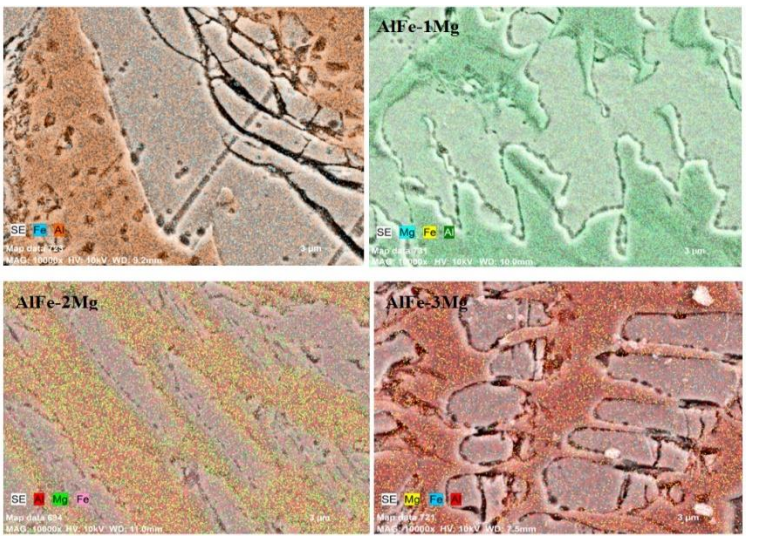

Figure 3. EDS mapping analyses of the casting samples for Al-Fe ve Al-Fe-xMg (x=1, 2, 3wt.%) alloys.

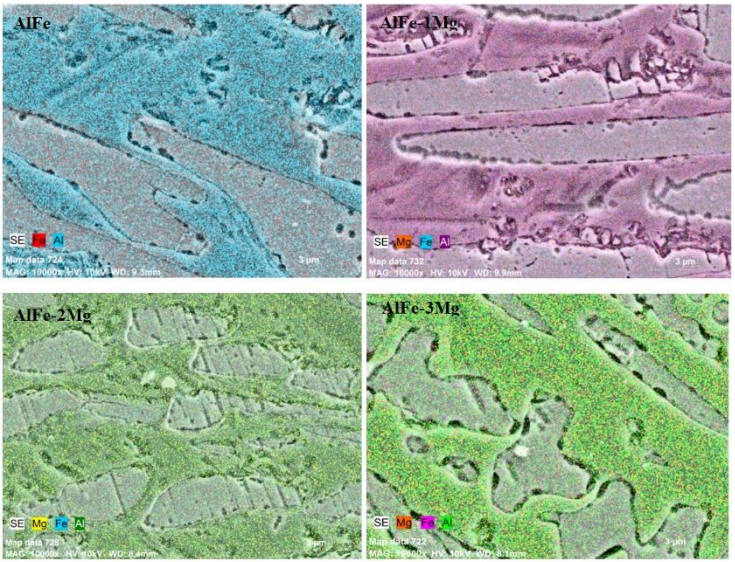

Figure 4. EDS mapping analyses of the homogenized samples for Al-Fe ve Al-Fe-xMg (x=1, 2, 3 wt.%) alloys.

Corrosion properties

Weight loss (mg/dm^2)-Time (hour) graphs of the examined alloys after immersion corrosion tests are given in Figure 5. When Figure 5 is examined, the change in weight loss over time is linear and the weight loss of homogenized alloys increased significantly towards 24 hours compared to the cast alloys. In both cast and homogenized alloys, while the Al-Fe alloy exhibits the lowest weight loss for a given hour, the Al-Fe-3Mg alloy has the highest weight loss.

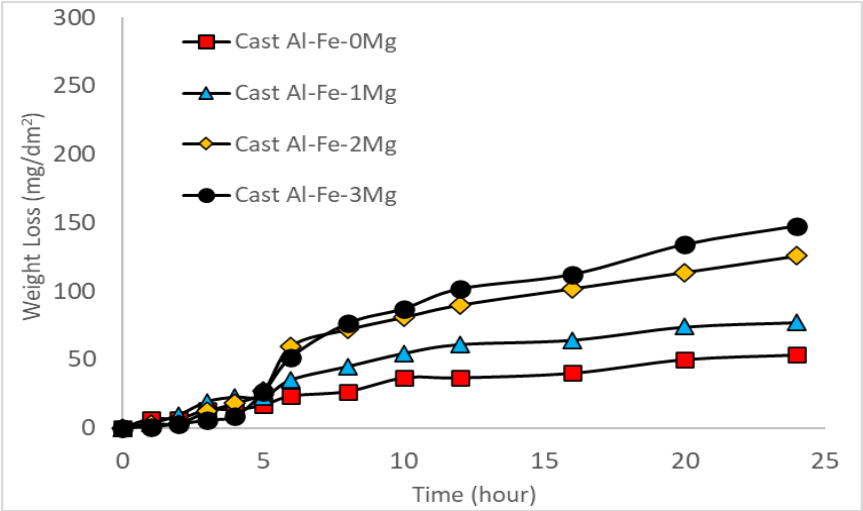

a)

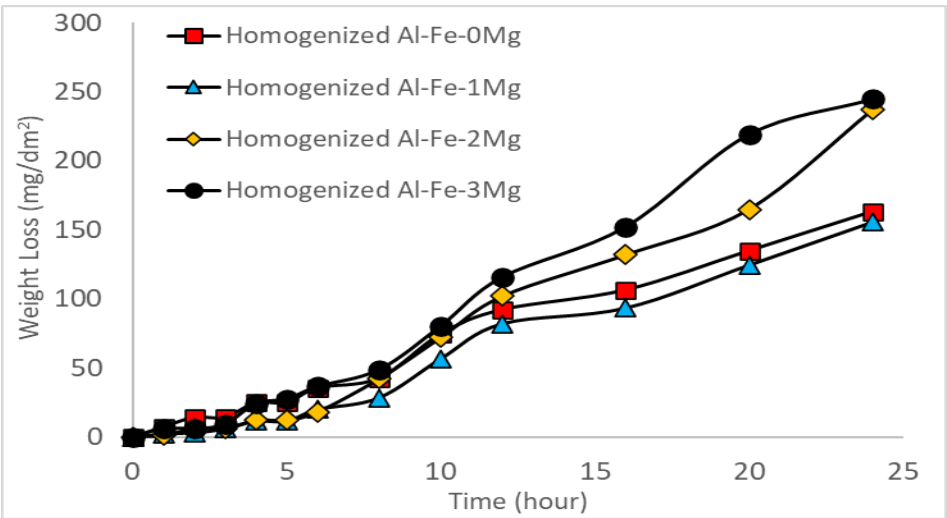

b)

Figure 5. Graphs of weight loss versus time (a) Cast alloys ve (b) Homogenized alloys.

When the weight loss results given in Figure 5 are divided to time (day), the corrosion rate expressed as mdd in mg/(dm^2*day) can be calculated. The changes versus time in corrosion rates of the examined alloys are given in Figure 6. Figure 6 shows that the corrosion rates of the examined alloys reached a steady state after the 12th hour, that is, they remained almost constant.

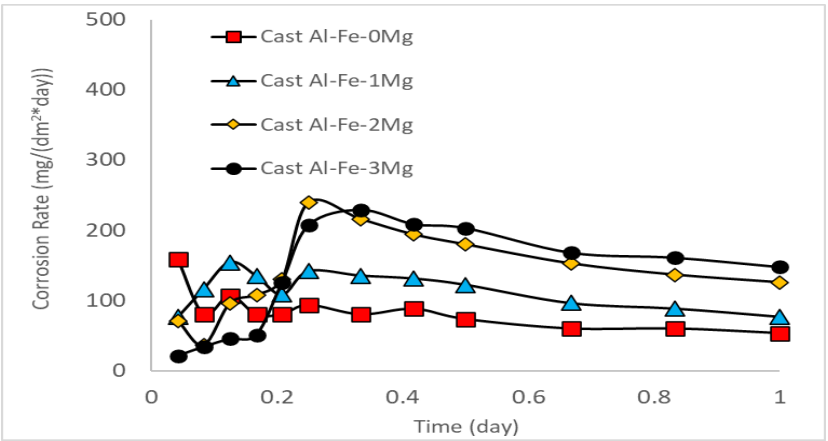

a)

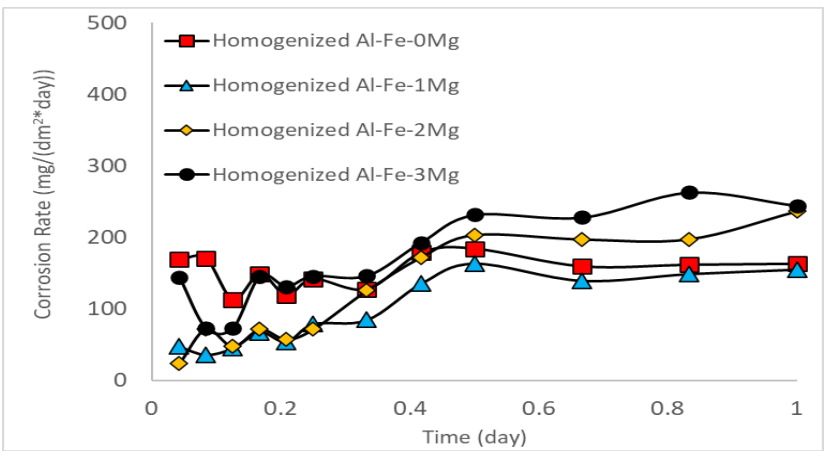

b)

Figure 6. Graphs of corrosion rates versus time (a) Cast alloys ve (b) Homogenized alloys.

Tafel curves, which are given as the change in current density (A/cm^2) and potential after the electrochemical corrosion test of the examined alloys, are given in Figure 7. When the Tafel curves given in Figure 7 are examined, it is observed that the curves are generally located in the active region (negative) and are arranged from left to right. By determining the corrosion potential and corrosion current values from the Tafel curves, the change graphs of the corrosion current and corrosion potential values with the Mg content of the alloy and are given in Figure 8.

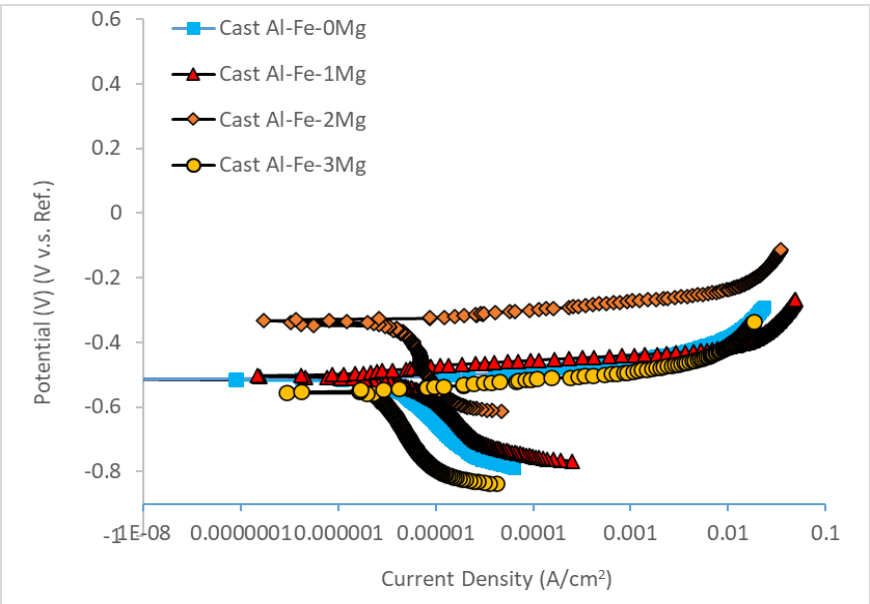

a)

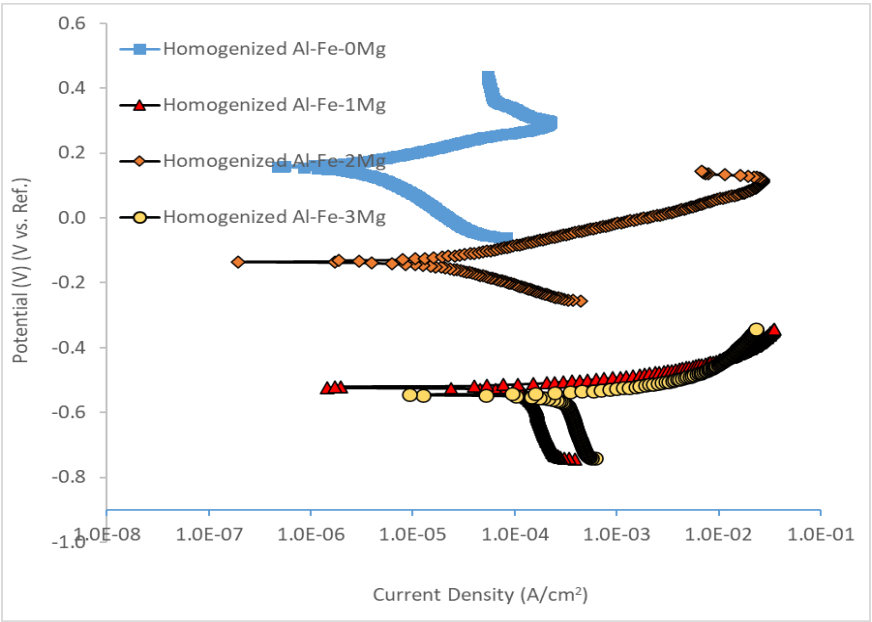

b)

Figure 7. Tafel Curves for (a) Cast alloys ve (b) Homogenized alloys.

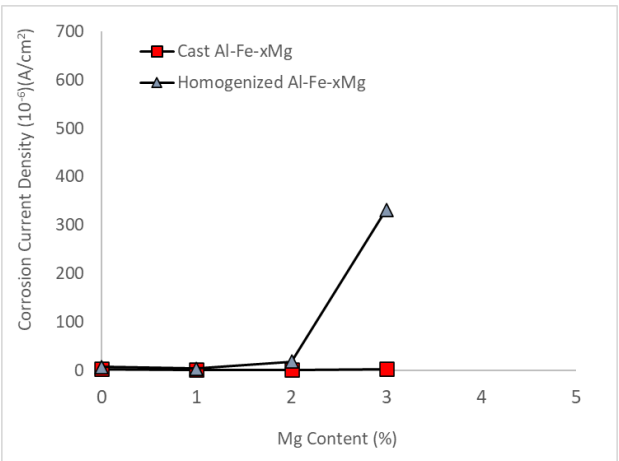

a)

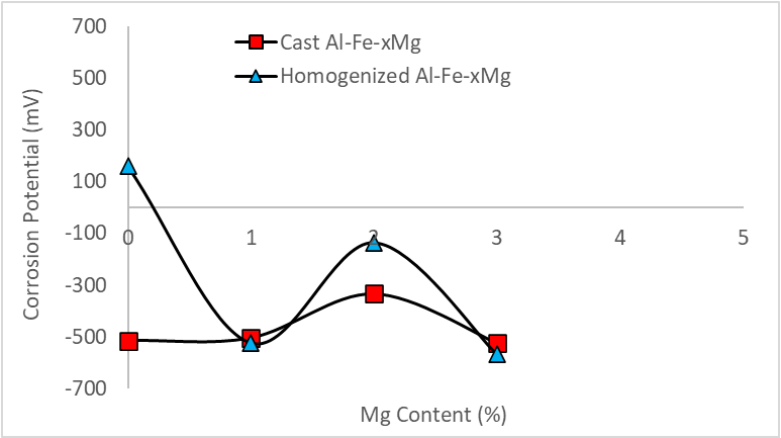

b)

Figure 8. (a) Change curves of corrosion current density with Mg content after electrochemical corrosion. (b) Change curves of corrosion potential with Mg content after electrochemical corrosion.

Figure 8 shows that the corrosion current density increases with increasing Mg content of the studied alloy, and for a certain alloy content, the corrosion density of the homogenized Al-Fe-xMg alloy is higher than that of the as-cast alloy. At high Mg contents of the alloy, the corrosion potential of the homogenized Al-Fe-xMg alloy is more negative than the corrosion potential of the as-cast alloy, supports the increase in the corrosion current density. The variation with the Mg content of corrosion rate values in mdd unit calculated using Faraday's law from corrosion current density data and corrosion rate values in constant mdd unit observed in Figure 6 is given in Figure 9.

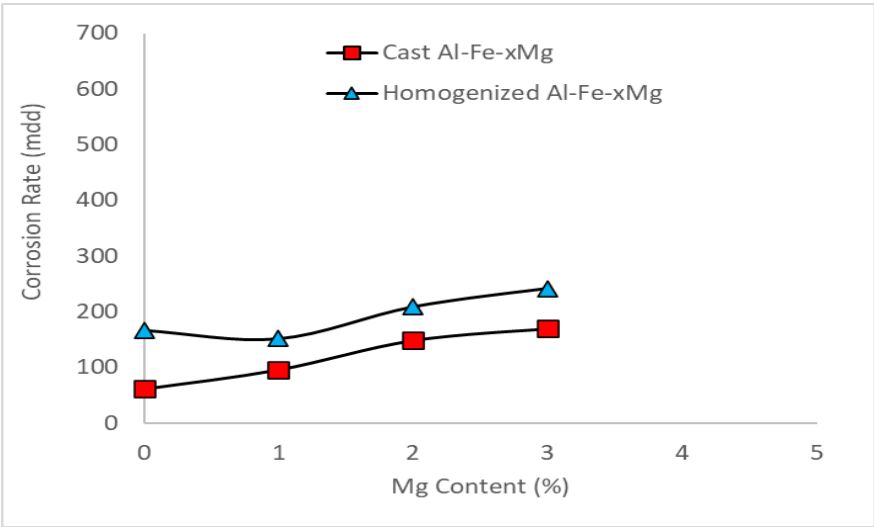

a)

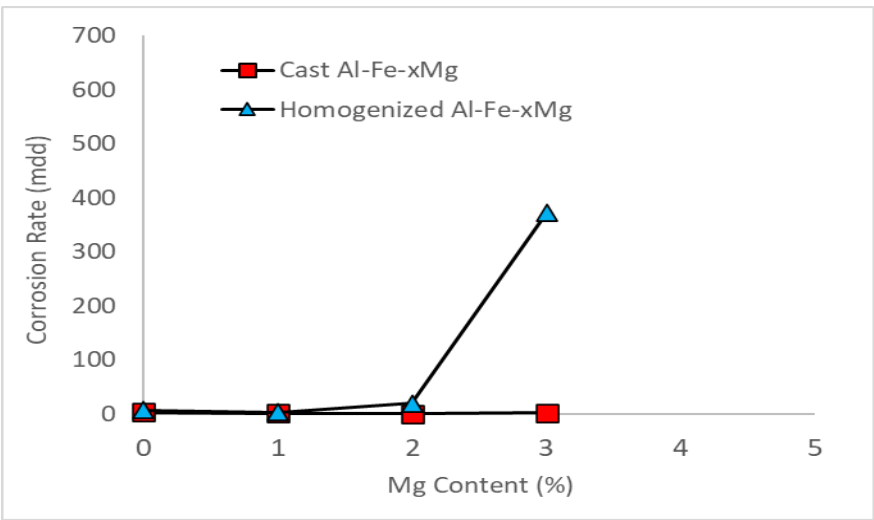

b)

Figure 9. Variation curves with Mg content of corrosion rate calculated in mdd unit after the (a) immersion and (b) electrochemical corrosion tests for examined alloys.

Both types of corrosion tests show that the corrosion rate of Al-Fe alloys with high Mg content increases significantly. It is thought that this situation is due to the Al_3Mg_2 intermetallics, the amount of which increases in the structure with the addition of Mg. As is known, Al_3Mg_2 is a common second phase in Mg-containing Al alloys. It is typically more active than Al and corrodes preferentially, causing localized corrosion (pitting, etc.), intergranular corrosion and stress corrosion cracking. When Al_3Mg_2 concentrates on grain boundaries, the formation of intergranular corrosion and stress corrosion cracking damage is a concern (Carroll et al., 2000; Jones et al., 2001; Searles et al., 2001). Dealloying and/or preferential dissolution manifests itself as the selective dissolution of the more active element of a homogeneous alloy and plays an important role in stress corrosion cracking and corrosion fatigue, as it can produce a highly brittle surface layer (Barnes et al., 2009; Deakin et al., 2004; Yasakau et al., 2007). Liu et al. (Liu et al., 2009; Liu et al., 2010) observed that Mg liberation occurred in Al_3Mg_2 intermetallics after immersion in NaCl solution. The selective corrosion reaction of Mg is given in Reaction 1.

$$4Al_3Mg_2 + 8H_2 \rightarrow 8MgH_2 + 12Al \qquad \text{(Reaction 1)}$$

The high corrosion resistance of the Mg-free Al-Fe alloy (Figure 9) can be attributed to the fact that the $Al_{13}Fe_4$ intermetallic formed in the structure (Figure 2) acts as a cathodic element on the surface of which the hydrogen ion is reduced and the formation of a passive film. Flores-Chan et al. (Flores-Chan et al., 2018) and Seikh et al. (Seikh et al., 2019) reported that led to the formation of a passive film and a dramatic reduction in the corrosion rate compared to pure Al for Al-Fe (20% by weight) alloys in an artificial seawater solution with NaOH solution in the range of pH values being basic (8, 10, 12 and 14) and for the addition of up to 10% Fe to the Al matrix in NaCl solution, respectively. In these studies (Flores-Chan et al., 2018; Seikh et al., 2019) were observed that the corrosion protection of Al-Fe alloys resulted from the formation of stable passive films (iron and aluminum hydroxide/aluminum ions) exposed to NaCl solution.

Additionally, Figure 9 shows that the corrosion rates of homogenized Al-Fe-xMg alloys are higher compared to the corrosion rates of Al-Fe-xMg alloys in cast form. This can be attributed to the microstructure of the casting alloys (Figure 2) being that the dendritic $Al_{13}Fe_4$ intermetallics are separate from each other, the $Al_{13}Fe_4$ intermetallics in the structure of the alloys are plate-shaped and continuous when homogenized, and the Al_3Mg_2 immetallic is distributed homogeneously in the matrix. During the corrosion experiment, the corrosion rate increased with the dissolution of the Al_3Mg_2 intermetallic, which was homogeneously distributed in the matrix and behaved anodicly, as a result of the cathodic reaction reduction of H^+ ions on the $Al_{13}Fe_4$ intermetallics, which had a plate shape in the structure of the homogenized Al-Fe-xMg alloys and whose surface area increased slightly. This situation was supported by the increase in the formation of cavities in the matrix and the $Al_{13}Fe_4$ intermetallic-matrix interface with the increased Mg content in the FESEM (Figure 10) examination performed after the immersion corrosion test. Corrosion damage occurs in the form of deep and superficial pits. The pit concentration increased with the Mg content of the alloy and the homogenization heat treatment.

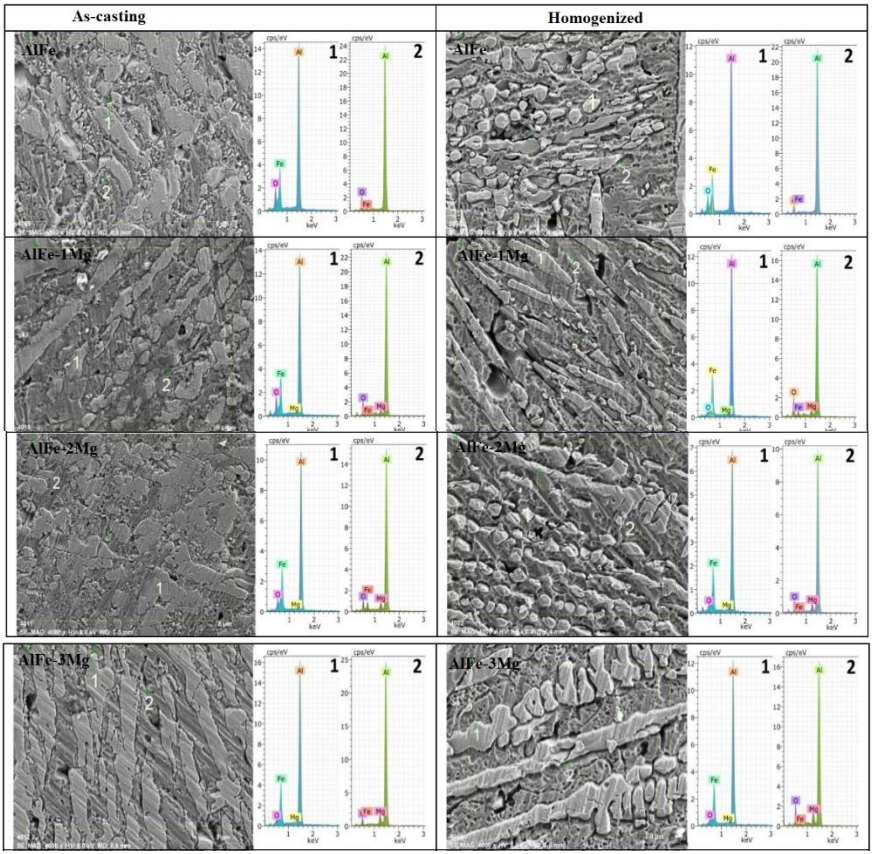

Figure 10. EDS analyzes taken from the areas determined during the FESEM examination after the immersion corrosion test of the examined alloys.

EDS analyzes taken from the areas determined during the FESEM examination after the immersion corrosion test of the examined alloys revealed the presence of Al, Fe, Oxygen peaks on the $Al_{13}Fe_4$ intermetallics and Al, Mg, Oxygen, Fe peaks on the matrix. EDS (Figure 10) results taken from the surfaces of Al-21,1Fe alloy after the corrosion test revealed the presence of Al, Fe and Oxygen peaks. This result indicates corrosion formation by the transformation of $Al_{13}Fe_4$ into Fe_2O_3, $Fe(OH)_2$ and $Al(OH)_3$ in region 1, and the transformation to $Al(OH)_3$ of the Al matrix in

region 2. It has also been reported by other researchers (Seri&Tagashira, 1990) that Al-Fe alloys provide protection against corrosion due to the formation of iron and aluminum hydroxide/oxide as a passive film exposed to NaCl solution. Liu et al. (Liu et al., 2010) reported that formed a surface film in the composition $AlMg_xO_{y1}(OH)_{y2}$ and that this film could also be expressed as $Al(OH)_3$, $Mg(OH)_2$, Al_2O_3 and MgO compounds, when Al_3Mg_2 intermetallic was exposed to a short-term solution based on XPS and ToF-SIMS data.

Reaction 2, which shows the dissolution of Mg, develops a hydrogen molecule for each dissolved Mg atom.

$Mg + 2H^- = Mg^{2+} + H_2$ (Total Reaction 2)

When the limited solubility of Mg^{2+} ions is exceeded, that is, at pH = 10.5 exhibited by a solution saturated with $Mg(OH)_2$, $Mg(OH)_2$ can be produced by Reaction 3 and/or by Reaction 4 at alkaline pH values:

$Mg^{2+} + 2OH^- = Mg(OH)^2$ (Product Formation Reaction 3)

$Mg + 2H_2O = Mg(OH)_2 + 2H + 2e^-$ (Anodic Film Formation 4)

Al can be passivated in neutral solutions with the help of Reaction 5 (Pourbaix, 1974):

$2Al + 3H_2O = Al_2O_3 + 6H^+ + 6e^-$ (Reaction 5)

Pourbaix (Pourbaix, 1974) listed five solids, including $Al(OH)_3$, in the E(V)-pH diagrams of pure Al in pure water, but noted that Al_2O_3 was formed because it had the lowest free energy. In contrast, in alkaline solutions, the aluminate ion is soluble and can form from solid Al by the following anodic partial reaction:

$Al + 2H_2O = AlO_2^- + 4H^+ + 3e^-$ (Reaction 6)

Pourbaix (Pourbaix, 1974) shows that adding acid to an aluminate solution forms a precipitate of $Al(OH)_3$ as follows:

$AlO_2^- + H^+ + H_2O = Al(OH)^3$ (Reaction 7)

It is important to understand here why the surface film contains $Al(OH)_3$ rather than Al_2O_3. Pourbaix (Pourbaix, 1974) stated that solid oxidized Al phases of Al_2O_3 have the lowest free energy and, as a result, is expected to occur during Al corrosion with partial anodic Reaction 5 for solutions with neutral pH values. However, since the pH value of the saturated solution with $Mg(OH)_2$ (Reaction 3 and Reaction 4) is approximately 10.5 (i.e. alkaline), Al corrodes to produce aluminate ions by the anodic partial reaction (Reaction 6) is expected. In other layers of the surface film, aluminate ions are expected to precipitate of $Al(OH)_3$ by Reaction 7. The presence of the Mg peak in the EDS analyzes at the Mg contents given in Figure 10 indicates that $Mg(OH)_2$ is formed according to Reaction 4, and as a result, the corrosion of the Al matrix containing Mg and Fe increases with the formation of aluminate ion AlO_2^- according to Reaction 6.

Conclusions

In this study, Al-21.1 wt% Fe alloy since it is rich in Fe and Fe has very low solid solubility in Al, insoluble Fe and Al+ $Al_{13}Fe_4$ phases, which will form a eutectic structure, were formed in the structure. With the application of homogenization annealing, Fe-rich $Al_{13}Fe_4$ intermetallic phases with different orientations were formed. With the addition of 0-3% Mg to the Al-21.1 Fe alloy, the corrosion rate increased by 45%. This is attributed to the formation of Al_3Mg_2 in the structure with the addition of Mg. The fact that the increase in corrosion rate is higher in homogenized Al-Fe-xMg alloys is due to the thinning and sphericalization of the $Al_{13}Fe_4$ intermetallicity, which acts cathodically. FESEM examination after the corrosion experiment revealed deep cavities at the $Al_{13}Fe_4$ intermetallic-matrix interface with galvanic coupling and shallow cavities on the matrix surface with the addition of Mg.

Acknowledge

This study was supported by Karabük University Scientific Research Projects Coordination with the project code KBÜBAP-18-

KP-009. The authors would like to thank the KBÜ-BAP unit for their financial support.

References

Barnes, A., Senior, N. A., & Newman, R. C. (2009). Film-induced cleavage of Ag-Au alloys. *Metallurgical and Materials Transactions A*, 40, 58-68.

Birol, Y. (2012). Effect of solute Mg on grain size of aluminium alloys. *Materials Science and Technology*, 28(8), 924-927.

Burger, G. B., Gupta, A. K., Jeffrey, P. W., & Lloyd, D. J. (1995). Microstructural control of aluminum sheet used in automotive applications. *Materials Characterization*, 35(1), 23-39.

Cao, X., & Campbell, J. (2004). The solidification characteristics of Fe-rich intermetallics in Al-11.5 Si-0.4 Mg cast alloys. *Metallurgical and Materials Transactions A*, 35, 1425-1435.

Carroll, M. C., Gouma, P. I., Mills, M. J., Daehn, G. S., & Dunbar, B. R. (2000). Effects of Zn additions on the grain boundary precipitation and corrosion of Al-5083. *Scripta Materialia*, 42(4), 335-340.

Che, H., Jiang, X., Qiao, N., & Liu, X. (2017). Effects of Er/Sr/Cu additions on the microstructure and mechanical properties of Al-Mg alloy during hot extrusion. *Journal of Alloys and Compounds*, 708, 662-670.

Cho, C. H., Son, H. W., & Hyun, S. K. (2020). Effect of Mg content on shear texture evolution at variable processing conditions in Al–Mg alloys. *Journal of Alloys and Compounds*, 825, 153927.

Cole, G. S., & Sherman, A. M. (1995). Light weight materials for automotive applications. *Materials Characterization*, 35(1), 3-9.

Deakin, J., Dong, Z., Lynch, B., & Newman, R. C. (2004). De-alloying of type 316 stainless steel in hot, concentrated sodium hydroxide solution. *Corrosion Science*, 46(9), 2117-2133.

Engler, O., Marioara, C. D., Hentschel, T., & Brinkman, H. J. (2017). Influence of copper additions on materials properties and corrosion behaviour of Al–Mg alloy sheet. *Journal of Alloys and Compounds*, 710, 650-662.

Fan, Z., Wang, Y., Zhang, Y., Qin, T., Zhou, X. R., Thompson, G. E., ... & Hashimoto, T. (2015). Grain refining mechanism in the Al/Al–Ti–B system. *Acta Materialia*, 84, 292-304.

Flores-Chan, J. E., Bedolla-Jacuinde, A., Patiño-Carachure, C., Rosas, G., & Espinosa-Medina, M. A. (2018). Corrosion study of Al–Fe (20 wt-%) alloy in artificial sea water with NaOH additions. *Canadian Metallurgical Quarterly*, 57(2), 201-209.

Hassani, A., Ranjbar, K., & Sami, S. (2012). Microstructural evolution and intermetallic formation in Al-8wt% Si-0.8 wt% Fe alloy due to grain refiner and modifier additions. *International Journal of Minerals, Metallurgy, and Materials*, 19, 739-746.

Hosseinifar, M., & Malakhov, D. V. (2008). Effect of Ce and La on microstructure and properties of a 6xxx series type aluminum alloy. *Journal of Materials Science*, 43, 7157-7164.

Ji, X., Zhang, H., Luo, S., Jiang, F., & Fu, D. (2016). Microstructures and properties of Al–Mg–SI alloy overhead conductor by horizontal continuous casting and continuous extrusion forming process. *Materials Science and Engineering: A*, 649, 128-134.

Jinta, M., Sakai, Y., Oyagi, M., Yoshizawa, S., Matsui, K., & Noda, K. (2000). Press forming analysis of aluminum auto body panel: wrinkle behavior in 5000 and 6000 series aluminum alloy sheet forming. *JSAE review*, 21(3), 407-409.

Jones, R. H., Baer, D. R., Danielson, M. J., & Vetrano, J. S. (2001). Role of Mg in the stress corrosion cracking of an Al-Mg alloy. *Metallurgical and Materials Transactions A*, 32, 1699-1711.

Khalifa, W., Samuel, F. H., & Gruzleski, J. E. (2003). Iron intermetallic phases in the Al corner of the Al-Si-Fe system. *Metallurgical and Materials Transactions A*, 34, 807-825.

Karabay, S. (2006). Modification of AA-6201 alloy for manufacturing of high conductivity and extra high conductivity wires with property of high tensile stress after artificial aging heat treatment for all-aluminium alloy conductors. *Materials & Design*, 27(10), 821-832.

Lui, A., Grant, P. S., Stone, I. C., & O'Reilly, K. A. Q. (2019). The role of grain refiner in the nucleation of AlFeSi intermetallic phases during solidification of a 6xxx aluminum alloy. *Metallurgical and Materials Transactions A*, 50(11), 5242-5252.

Liu, M., Zanna, S., Ardelean, H., Frateur, I., Schmutz, P., Song, G., ... & Marcus, P. (2009). A first quantitative XPS study of the surface films formed, by exposure to water, on Mg and on the Mg–Al intermetallics: Al_3Mg_2 and $Mg_{17}Al_{12}$. *Corrosion Science*, 51(5), 1115-1127.

Liu, M., Schmutz, P., Zanna, S., Seyeux, A., Ardelean, H., Song, G., ... & Marcus, P. (2010). Electrochemical reactivity, surface composition and corrosion mechanisms of the complex metallic alloy Al_3Mg_2. *Corrosion Science*, 52(2), 562-578.

Lloyd, D. J., & Court, S. A. (2003). Influence of grain size on tensile properties of Al-Mg alloys. *Materials Science and Technology*, 19(10), 1349-1354.

McNelley, T. R., & Hales, S. J. (1995). McNelley, Grain Boundary Misorientation Distribution and Superplasticity and Superplastic Forming II, ed. by A. K. Ghosh and T. R. Bieler, TMS Annual Meeting, Las Vegas, NV, 57 (1995).

Mostafaei, M. A. (2019). Serrated yielding behavior after cold and hot rolling of a high Mg content Al–Mg alloy. *Journal of Alloys and Compounds*, 811, 151997.

Pourbaix, M. (1974). *Atlas of Electrochemical Equilibria in Aqueous Solutions*, NACE, Houston, Texas,USA, Cebelcor/Brussels.

Que, Z., Zhou, Y., Wang, Y., Mendis, C. L., & Fan, Z. (2021). Effects of Mg addition on the Al_6(Fe, Mn) intermetallic compounds and the grain refinement of α-Al in Al-Fe-Mn alloys. *Materials Characterization*, 171, 110758.

Que, Z., Zhou, Y., Wang, Y., & Fan, Z. (2017). Composition templating for heterogeneous nucleation of intermetailic compounds. Proceedings of the 6th Decennial International Conference on Solidification, Windsor, UK, 25-27 July, pp. 1 - 5.

Que, Z., Wang, Y., & Fan, Z. (2018). Formation of the Fe-containing intermetallic compounds during solidification of Al-5Mg-2Si-0.7 Mn-1.1 Fe alloy. *Metallurgical and Materials Transactions A*, 49, 2173-2181.

Samuel, A. M., & Samuel, F. H. (1997). Modification of iron intermetallics by magnesium and strontium in Al-Si alloys. *International Journal of Cast Metals Research*, 10(3), 147-157.

Sauvage, X., Bobruk, E. V., Murashkin, M. Y., Nasedkina, Y., Enikeev, N. A., & Valiev, R. Z. (2015). Optimization of electrical conductivity and strength combination by structure design at the nanoscale in Al–Mg–Si alloys. *Acta Materialia*, 98, 355-366.

Searles, J. L., Gouma, P. I., & Buchheit, R. G. (2001). Stress corrosion cracking of sensitized AA5083 (Al-4.5Mg-1.0Mn). *Metallurgical and Materials Transactions A*, 32, 2859-2867.

Sheppard, T., Parson, N. C., & Zaidi, M. A. (1983). Dynamic recrystallization in Al–7Mg alloy. *Metal Science*, 17(10), 481-490.

Seikh, A. H., Baig, M., Singh, J. K., Mohammed, J. A., Luqman, M., Abdo, H. S., ... & Alharthi, N. H. (2019). Microstructural and corrosion characteristics of Al-Fe alloys

produced by high-frequency induction-sintering process. *Coatings*, 9(10), 686.

Seri, O., & Tagashira, K. (1990). The interpretation of polarization curves for Al-Fe alloys in de-aerated NaCl solution. *Corrosion Science*, 30(1), 87-94.

Shabestari, S. G., & Ghanbari, M. (2010). Effect of plastic deformation and semisolid forming on iron–manganese rich intermetallics in Al–8Si–3Cu–4Fe–2Mn alloy. *Journal of Alloys and Compounds*, 508(2), 315-319.

Smith, T., O'Reilly, K., Kumar, S., & Stone, I. (2013). Influence of grain-refiner addition on the morphology of Fe-bearing intermetallics in a semi-solid processed Al-Mg-Si alloy. *Metallurgical and Materials Transactions A*, 44, 4866-4871.

Suárez-Peña, B., & Asensio-Lozano, J. (2006). Influence of Sr modification and Ti grain refinement on the morphology of Fe-rich precipitates in eutectic Al–Si die cast alloys. *Scripta Materialia*, 54(9), 1543-1548.

Taleff, E. M., Lesuer, D. R., & Wadsworth, J. (1996). Enhanced ductility in coarse-grained Al-Mg alloys. *Metallurgical and Materials Transactions A*, 27, 343-352.

Toros, S., Ozturk, F., & Kacar, I. (2008). Review of warm forming of aluminum–magnesium alloys. *Journal of Materials Processing Technology*, 207(1-3), 1-12.

Valiev, R. Z., Murashkin, M. Y., & Sabirov, I. (2014). A nanostructural design to produce high-strength Al alloys with enhanced electrical conductivity. *Scripta Materialia*, 76, 13-16.

Wang, M., Xu, W., & Han, Q. (2016). Study of refinement and morphology change of AlFeSi phase in A380 alloy due to addition of Ca, Sr/Ca, Mn and Mn, Sr. *Materials Transactions*, 57(9), 1509-1513.

Yasakau, K. A., Zheludkevich, M. L., Lamaka, S. V., & Ferreira, M. G. (2007). Role of intermetallic phases in localized corrosion of AA5083. *Electrochimica Acta,* 52(27), 7651-7659.

Yuan, W., & Liang, Z. (2011). Effect of Zr addition on properties of Al–Mg–Si aluminum alloy used for all aluminum alloy conductor. *Materials & Design,* 32(8-9), 4195-4200.

Zhang, Y., Jie, J., Gao, Y., Lu, Y., & Li, T. (2013). Effects of ultrasonic treatment on the formation of iron-containing intermetallic compounds in Al-12%Si-2%Fe alloys. *Intermetallics,* 42, 120-125

CHAPTER II

Comparative Strength Analysis of PLA, ABS, PETG, TPU, and ASA Filaments: Influence of Nozzle Size and Filling Parameters

Sedat ÇELİK[1]
Mehmet Masum TÜNÇAY[2]
Görkem YUMUŞAK[3]

Introduction

Layer-by-layer deposition of thermoplastic polymers including PLA, ABS, PETG, ASA, and TPU is a component of the additive manufacturing process known as FDM. These thermoplastic substances are employed to produce 3D things. More importantly,

[1] Grad Student (Engineer), Marmara University, Metallurgical and Materials Engineering, 34854, Istanbul, Türkiye, ORCID: 0009-0009-0359-5322
[2] Asst. Prof., Marmara University, Metallurgical and Materials Engineering, 34854, Istanbul, Türkiye, ORCID: 0000-0002-1624-5454
[3] Asst. Prof., Marmara University, Metallurgical and Materials Engineering, 34854, Istanbul, Türkiye, E-mail: gorkem.yumusak@marmara.edu.tr, ORCID: 0000-0002-5047-4357

FDM techniques produce intricate, complex parts while being clean, safe, and able to be completed at home. FDM's operating premise is simple to understand but crucial. A thermoplastic material is first heated and then forced through an extruder as part of the process. The extruded and melted filament is pushed to the floor from the nozzle, which is equipped with a heat control unit and is set to a specified temperature, and the process is repeated layer by layer until the desired 3D materials are formed. It is crucial to note that all 3D parts created using the FDM technique are derived from drawings created in CAD software (Mohamed et al., 2015). As the word "additive" implies, 3D printing is an additive manufacturing process and is based on the idea of stacking layers to create a physical shape. More intricate and complicated structures, whether they are small, functional, or larger, can be generated more quickly and with a cheaper, more effective setup as compared to other traditional technologies. It is very practical and extensively used in the engineering area when it comes to creating lightweight geometries. The quality and shape of the finished work are significantly influenced by the working settings (Bellini et al., 2003). They will have different qualities than components made using other sets of process settings, even when they have the same geometry. These parameters can be divided into two categories: working parameters and machine parameters. Nozzle, bed, and nozzle diameter temperatures are machine parameters. Working parameters include build orientations, raster width, and angle (Kristiawan et al., 2021). The build orientation, layer thickness, and FDM parameters are shown in the above figure. Each of them individually has a different impact on the final product.

FDM process parameter optimization and conditions are crucial for enhancing surface roughness, material behavior, dimensional accuracy, mechanical characteristics, and build time. Literature searches and reviews are done to comprehend and explain the significance in terms of FDM. The impact of these characteristics and their optimization on the end product's quality is also very significant. By setting parameters that must be optimized, a higher

surface quality can be achieved. A material with good surface characteristics typically requires less post-production expense. Accordingly, Thrimurthulu et al. contend that a thin layer thickness is necessary to produce a high-quality surface finish (Thrimurthulu et al., 2004). A related investigation by Horvath (Horvath et al., 2007) looked at the layer thickness, the visible surface, and the extrusion temperature. Their findings were contrasted with those of Vasudevarao, who investigated how build orientation, raster width, layer thickness, air gap, and model temperature affected surface roughness (Vasudevarao et al., 2000). The impact of six parameters on surface roughness and dimensional accuracy was also studied by Wang et al. (Chung Wang et al., 2007). Layer thickness emerged as one of these parameters that had the greatest influence on surface roughness while building orientation in the Z-direction had a notable impact on dimensional accuracy. Additionally, Bakar (Bakar et al., 2010) examined internal raster, shell width, and layer thickness to determine their significance in enhancing surface polish.

Mechanical properties are unquestionably significant and easily influenced by changes in process parameters under various FDM settings. FDM-printed parts do not have the same qualities as filaments because there are many different parameters. As a result, it is important to think about and assess how process parameters may affect tensile, compression, and flexural stress. According to Wang's investigation of the effects of six distinct processes, build orientation on Z-direction had the greatest impact on tensile strength (Chung Wang et al., 2007). Panda considered the process characteristics of layer thickness, build orientation, raster orientation, raster width, and air gap and their effects on tensile strength and created a quadratic equation to comprehend their effects (Panda et al., 2009). Conclusion: Every parameter, except for raster width, affects tensile strength. Es looked into the tensile characteristics of ABS-made parts while maintaining raster orientation as a variable (Es-Said et al., 2000). Building an ABS structure for tissue engineering, Ang looked at the effects of various process variables, including air gap, raster width, build orientation, build layer, and build profile (Chin

Ang et al., 2006). Air gap and raster width were the two factors that had the greatest impact on compressive strength among all of these other factors. Lower and upper levels, respectively, were ideal settings for both parameters in terms of compressive strength optimization. Based on the findings of their PLA part production and statistical analysis, Luzanin concluded that layer thickness and the link between construction orientation and infill density had a significant impact on flexural strength (Lužanin et al., 2014). Raut studied the impact of build orientation on flexural strength, and like previous studies, their findings indicated that a 00 build orientation maximizes flexural strength (Raut et al., 2014). Comparing the tensile, compressive, and flexural properties of PEEK and ABS, Wu found that the flexural strength was comparable in cases where the tensile and compressive properties could be distinguished (Wu et al., 2015).

Filament is a specific kind of thermoplastic material created for 3D printers. It is made by converting granular material into plastic wire by putting it through a variety of processes. This thread has been expertly wrapped using cutting-edge methods to resemble a spool. Despite the process' seeming simplicity, tremendous caution must be exercised from the granule to the filament to the winding stage. Ensuring a smooth and steady flow of filament throughout its application within the 3D printer is a vital aspect directly affecting the quality of the end-generated product. Because it comes in several types, colors, and diameters, the filament may be customized and used in a variety of ways during the 3D printing process. There are numerous filament types available today, each with a unique set of mechanical characteristics and colors. PLA's popularity has increased significantly as a result of its effective production from renewable resources. By 2021, it will have surpassed all other bioplastics in terms of volume consumed globally. Due to its exceptional characteristics, which include a low melting point, high strength, minimal thermal expansion, reliable layer adhesion, and better heat resistance when subjected to annealing, it is the finest choice for this application. Comparing PLA to other popular 3D

printing polymers, it also has the lowest intrinsic heat resistance in its unannealed state (Nagarajan et al., 2016). ASA is a type of amorphous thermoplastic polymer. Because it is a thermoplastic, it can be melted and reshaped. Throughout this procedure, it keeps all of its physical properties. It is a recyclable material. The high-performance thermoplastic Acrylonitrile Styrene Acrylate, often known as ASA filament, is similar to ABS and has outstanding UV resistance, making it suitable for use in outdoor applications. Thermoplastic polyurethane (TPU), which is categorized as polyurethane plastic, is a member of the thermoplastic elastomer (TPE) family. It blends the plastic's durability and rubber's elasticity. The thermoplastic material ABS, also known as Acrylonitrile Butadiene Styrene, provides excellent moldability when heated and homogeneous hardening when cooled. Due to its versatility and steady performance in traditional production across multiple industries, as well as among enthusiasts of 3D printing, ABS filament has a wide range of uses. Polyethylene Terephthalate Glycol, or PETG, is a material that is frequently used in 3D printing. It performs the role of a PET modification. The substance that successfully lowers PETG's melting point and ensures its convenient use in 3D printing processes is glycol. These characteristics make PETG the perfect filament to use for printing objects that will be utilized in hostile environments or that will be put under a lot of physical stress.

Materials and Method

Experiments have been done with a machine obeying ISO 527 standards which refers to general principles for obtaining tensile properties of plastics and plastic composites under certain conditions. We can get results of tensile stress, strain, tensile modulus, yield point, point of break, and poisons ratio under that standard. In tensile tests, outcomes are varied on a defined specimen and the pull-off speed of that specimen. For component design, the result may be a trustworthy base, but suitability is limited because measurement results on standardized specimens generally result

under altered strain rates. The testing machine, represented in Figure 1, measures 2 different values which are force and extension. The machine is connected to a computer and there is software that shows values that are measured on the tensile test machine. Specimens' length and width are measured, and it is tucked into two sides of the testing machine from up and from the bottom. It is important to connect material properly or else it will slip from the tucked area. The length between two connection points is again measured and entered into the system. Before testing, the name of the material and the number of tests is that applied have to be entered into the software. After that, the results of previously done tests must have been cleaned to prevent any complications. The last step before starting to test is vital because the gained results correlate with that step directly, pull-of speed must be set as required. In our experiment, it was set to 5 mm/min. After all needs have been met, it is permitted to carry on with the test.

Figure 1: *Tensile Test Device*

According to the ASTM standards our specimen has an inner circle width of 13 mm and outer circle width of 19 mm. From the left-hand side to the right-hand side, the length of the specimen is 165 mm, and the length between the necks of the specimen is 57 mm. It has a height of 3.2 mm. Figure 2 shows the PETG, ASA, TPU, PLA, and ABS printed specimens that we utilized in the tensile test. The photographs were taken just before the tensile test, just before the specimens broke. Nozzle diameter and infill density are taken into account and handled as variable parameters while creating such samples. The nozzle diameters are set to 1 mm and 0.4 mm, respectively, with infill densities of 50% and 100%. For instance, we have nozzle diameters of 1 mm and 0.4 mm for 50% and 100% of the infill density, respectively. We have four separate samples for each infill density.

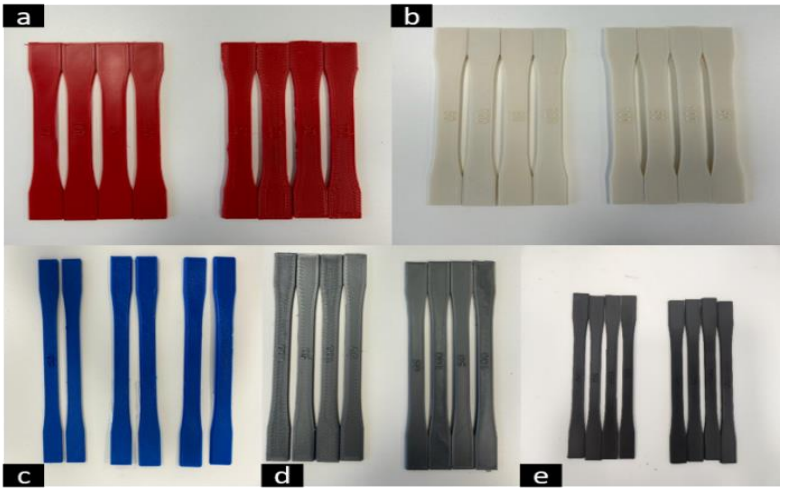

Figure 2: *a-) PETG, b-) ASA, c-) TPU, d-) PLA, e-) ABS printed specimens*

3D Working Parameters

The machines shown in Figure 3 were used to take prints of the samples that would be put through a tensile test. Table 1 provides detailed information on the 3D printer specifications needed for printing.

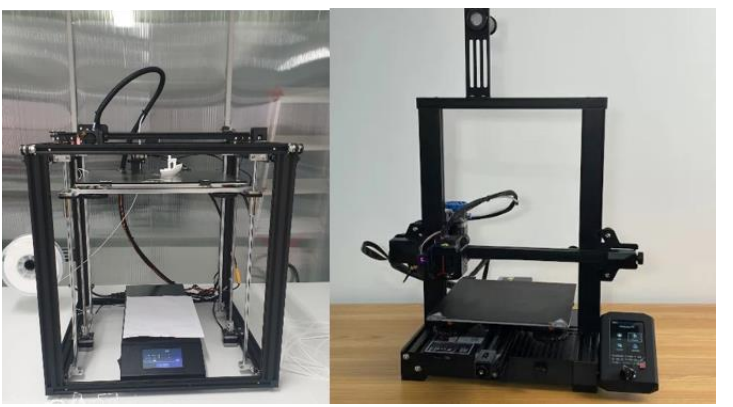

Figure 3: *Creality ender 5 plus and ender 3 v2*

Table 1: *3D Working Parameters*

Manufacturing/Design parameter	**ABS**	**ASA**	**PLA**	**PETG**	**TPU**
Nozzle temperature	260 °C	260 °C	200 °C	240 °C	200 °C
Bed temperature	110 °C	110 °C	60 °C	70 °C	60 °C
Nozzle diameter	0.4 mm and 1 mm				
Infill pattern	Gyroid				
Infill percentage	100% and 50%				
Filament diameter	1.75 mm				
Layer height	0.2 mm				
Top and Bottom Layers	4				
Cooling	Fan cooling				
Printing speed	50 mm/s				

By using the Ultimaker Cura application to slice the models and input the required infill and nozzle parameters, the samples were created. Figures 4, 5, 6, and 7 are included.

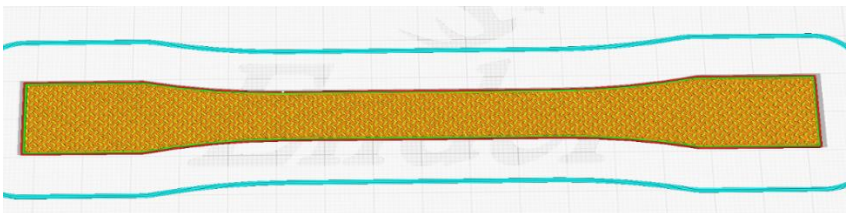

Figure 4: *Layer view of the sample with 0.4 mm nozzle size and 50% infill*

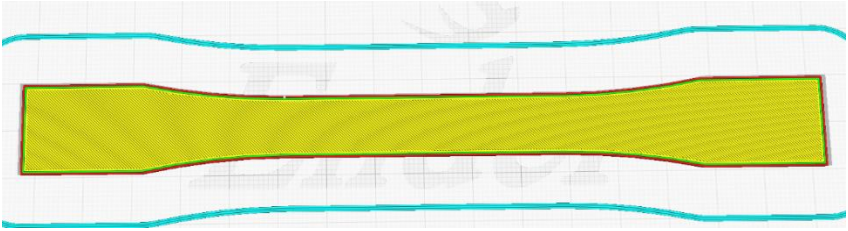

Figure 5: *Layer view of the sample with 0.4 mm nozzle size and 100% infill*

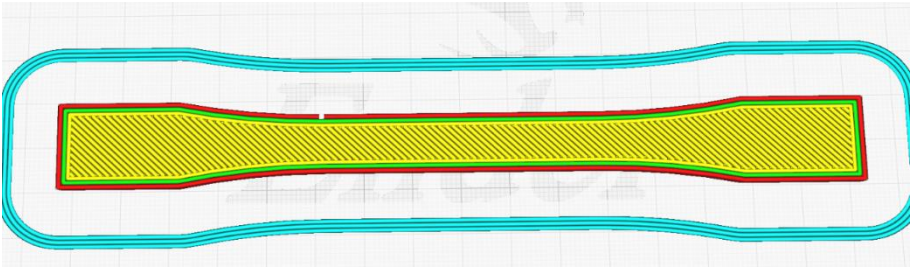

Figure 6: *Layer view of the sample with 1 mm nozzle size and 50% infill*

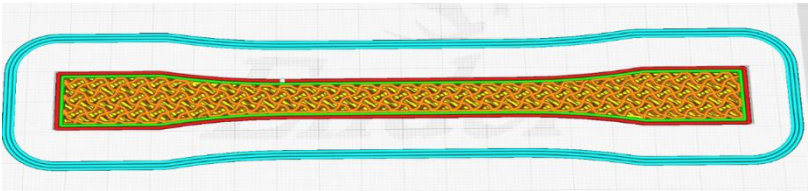

Figure 7: *Layer view of the sample with 1 mm nozzle size and 50% infill*

Results and Discussion

Nozzle size and infill density were changeable variables in this experiment. Nozzle sizes were chosen to be 0.4 mm and 1 mm, with infill densities varying between 50% and 100% for each size. For additional analysis, tensile tests are performed on every specimen made of PLA, ABS, ASA, PETG, and TPU. The results of the tests

are displayed in Table 2, Table 3, Table 4, and Table 5 for various nozzle diameters.

Table 2: *0.4 mm Nozzle size and 50 % infill density*

	Filament Type	Elongation %	Tensile Strength N/mm^2
Nozzle size 0.4 mm and Infill 50%	PLA	9,00	41,61
	PETG	10,25	37,65
	ABS	10,65	31,01
	ASA	10,90	27,25
	TPU	Data could not be obtained	

Table 3: *0.4 mm Nozzle size and 100% infill density*

	Filament Type	Elongation %	Tensile Strength N/mm^2
Nozzle size 0.4 mm and Infill 100%	PLA	9,7	57,135
	PETG	11,6	49,31
	ABS	8,8	37,29
	ASA	10,1	36,74
	TPU	Data could not be obtained	

Increases in infill density from 50% to 100% significantly enhance each specimen's tensile strength, with PLA specimens showing the largest differences, per obtained results in Table 3 for 0.4 mm nozzle size. The elongation of ABS and ASA, however, is lowered while that of PLA and PETG is increased.

Table 4: *Nozzle size 1.0 mm and Infill 100% infill density*

	Filament Type	Elongation %	Tensile Strength N/mm^2
Nozzle size 1.0 mm and Infill 100%	PLA	10,20	63,56
	PETG	11,95	56,02
	ABS	9,40	47,78
	ASA	12,45	43,025
	TPU	Data could not be obtained	

Tensile strength is once more enhanced with an increase in infill density from 50% to 100% for a 1.0 mm nozzle size (table 4), however, this time changes are more subtle. Elongation also saw changes; whereas PLA and ASA elongated more, PETG and ABS elongated less. The tensile strength of the material grows dramatically with increasing nozzle size and constant infill density, but again, elongation does not rise for each one of them when comparisons for the effect of nozzle size are made. The following graphics explain the fluctuation in tensile strength and elongation with increasing nozzle size. The correlation between elongation and tensile force is illustrated in Figure 8, Figure 9, Figure 10, and Figure 11 categorized by filament type, for samples with four different parameters.

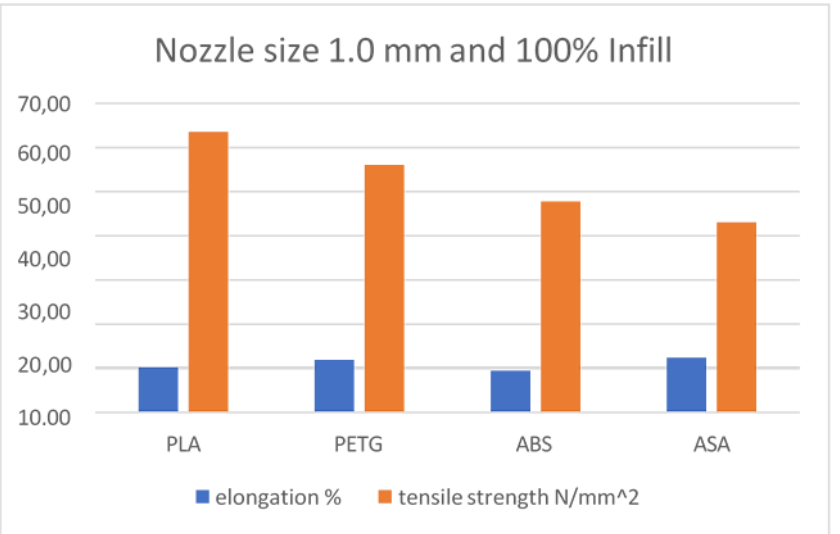

Figure 8: *According to nozzle Size 1.0 mm and 100% Infill, filaments compared*

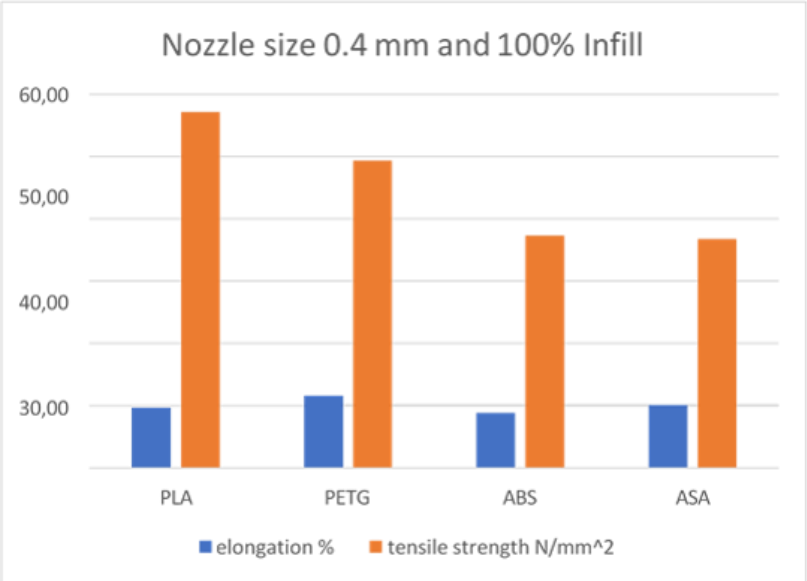

Figure 9: *According to nozzle Size 0.4 mm and 100% Infill, filaments compared*

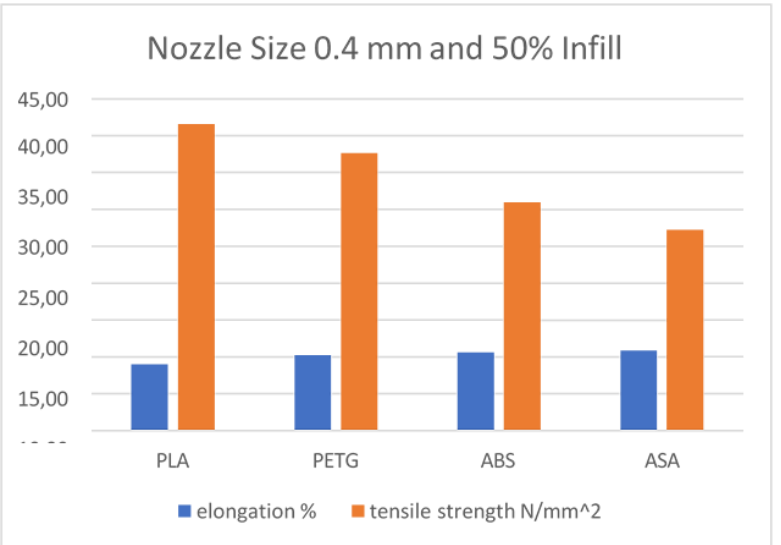

Figure 10: *According to nozzle Size 0.4 and 50% Infill, filaments compared*

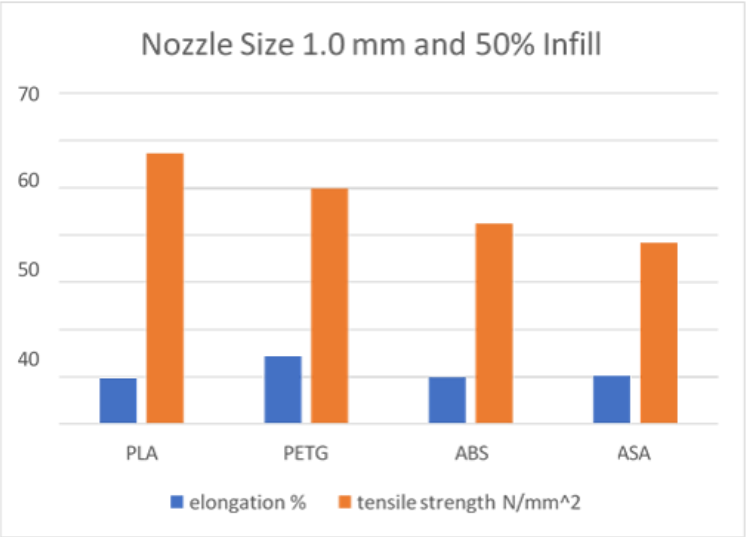

Figure 11: *According to nozzle Size 1.0 mm and 50% Infill, filaments compared*

Figure 12, and Figure 13 present the comprehensive test results for PLA filament samples. Two tests have been conducted for each infill density, and their averages are used. The average tensile strength improved from 57.2 to 63.5 for 1mm nozzle diameter, and the average elongation increased from 9.65 to 10.2.

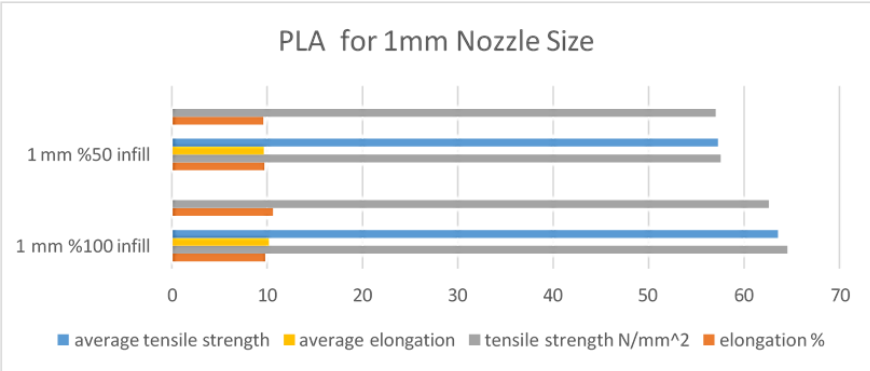

Figure 12: *PLA for 1mm Nozzle Size*

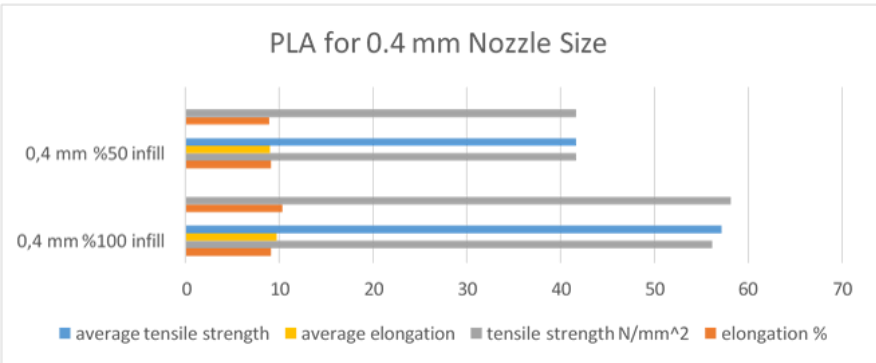

Figure 13: *PLA for 0.4 mm Nozzle Size*

The average tensile strength improved from 41.6 to 57.1 for 0.4 mm nozzle size and from 50% to 100% for infill density, while the average elongation increased from 9 to 9.7. Figure 14 and Figure 15 presents the comprehensive test results for ABS filament samples. The average tensile strength improved from 42.4 to 47.7 in the ABS results for 1mm nozzle size, but average elongation decreased from 9.9 to 9.4 as infill increased from 50% to 100%.

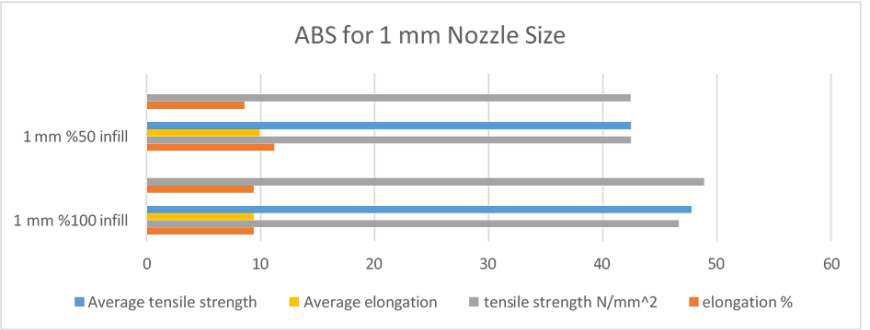

Figure 14: *ABS for 1 mm Nozzle Size*

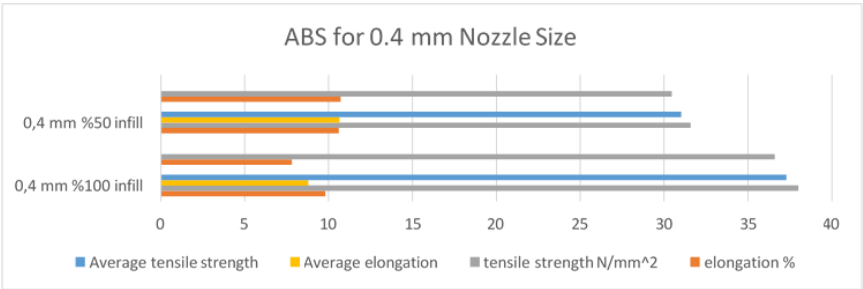

Figure 15: *ABS for 0.4 mm Nozzle Size*

Average tensile strength rose from 31.0 to 37.3 for printed ABS specimens with 0.4 mm nozzle sizes, while average elongation dropped from 10.7 to 8.8. Figure 16 and Figure 17 presents the comprehensive test results for ASA filament samples. The average tensile strength of ASA for 1mm nozzle size rose from 38.4 to 43 while infill was raised from 50% to 100%. Elongation on average increased from 10.2 to 12.45. Average tensile strength rose from 27.2 to 36.7 for printed ASA specimens with 0.4 mm nozzle sizes, while average elongation dropped from 10.9 to 10.1.

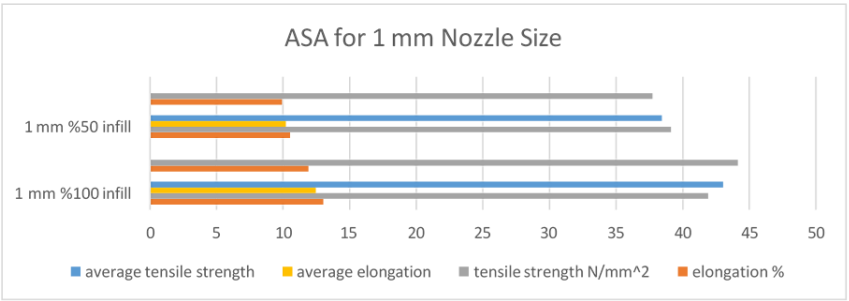

Figure 16: *ASA for 1 mm Nozzle Size*

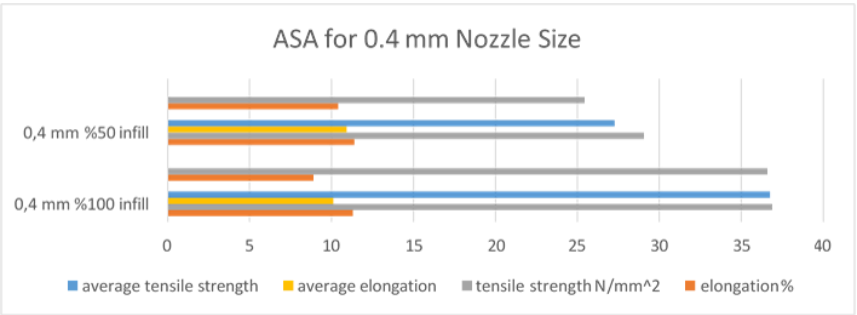

Figure 17: *ASA for 0.4 mm Nozzle Size*

Figure 18 and Figure 19 presents the comprehensive test results for PETG filament samples. While average tensile strength improved for PETG for 1mm nozzle size while increasing infill from 50% to 100%, average elongation decreased from 14.4 to 11.95. Average tensile strength rose from 34.6 to 49.3 for printed ASA specimens with 0.4 mm nozzle sizes, while average elongation dropped from 10.2 to 11.6.

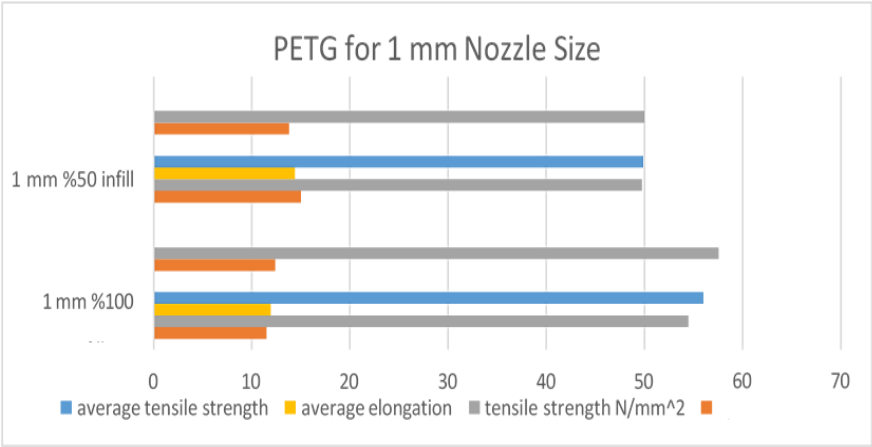

Figure 18: *PETG for 1 mm Nozzle Size*

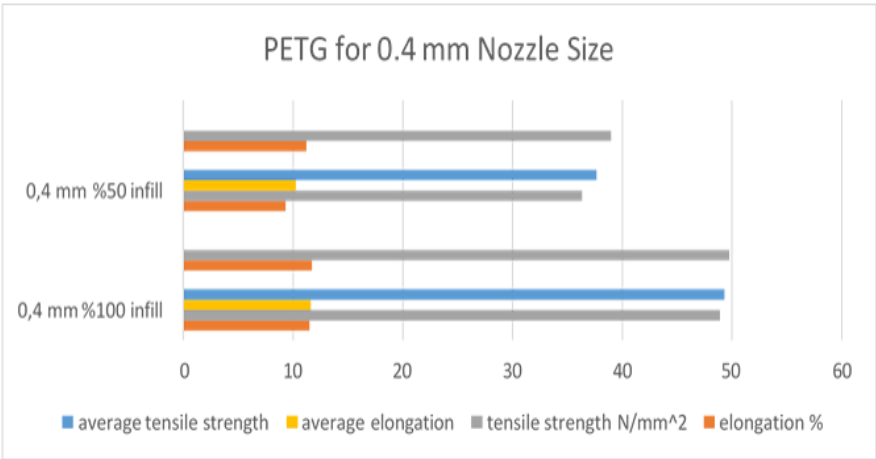

Figure 19: *PETG for 0.4 mm Nozzle Size*

Samples prepared with TPU filament were subjected to the same standard tensile test as samples produced from other filaments. During the test, elongation up to 1000% was observed; however, despite exceeding the machine limits, no fracture occurred. This situation led to the inability to obtain the necessary data for the tensile test.

Conclusions

The goal of the experiment was to determine how the infill density and nozzle size impacted the tensile strength and elongation of specimens made using a range of 3D printing materials, including PLA, ABS, ASA, PETG, and TPU. The results showed that, for a 0.4 mm nozzle size, boosting the infill density from 50% to 100% significantly increased the tensile strength of all specimens, with PLA showing the most difference. Although the elongation varied between the various materials, PLA and PETG showed an improvement while ABS and ASA showed a decline. When the infill density was increased from 50% to 100%, similar results were obtained with a 1.0 mm nozzle size. This time, though, there were variations in the tensile strength and elongation. Elongation decreased for PETG and ABS while increased for PLA and ASA. When the effects of nozzle size were compared, it was discovered that increasing the nozzle size while maintaining a constant infill density significantly increased the materials' tensile strength but did not always increase elongation. Overall, the experimental results show how these effects rely on the materials used and shed light on how nozzle size and infill density affect the mechanical properties of 3D-printed objects.

References

Bakar, N. S. A., Alkahari, M. R., & Boejang, H. (2010). Analysis on fused deposition modelling performance. *Journal of Zhejiang University-Science A*, 11, 972–977.

Bellini, A., & Güçeri, S. (2003). Mechanical characterization of parts fabricated using fused deposition modeling. *Rapid Prototyping Journal*, *9*(4), 252–264.

Chin Ang, K., Fai Leong, K., Kai Chua, C., & Chandrasekaran, M. (2006). Investigation of the mechanical properties and porosity relationships in fused deposition modelling-fabricated porous structures. *Rapid Prototyping Journal*, 12(2), 100–105.

Chung Wang, C., Lin, T., & Hu, S. (2007). Optimizing the rapid prototyping process by integrating the Taguchi method with the Gray relational analysis. *Rapid Prototyping Journal*, 13(5), 304–315.

Es-Said, O. S., Foyos, J., Noorani, R., Mendelson, M., Marloth, R., & Pregger, B. A. (2000). Effect of layer orientation on mechanical properties of rapid prototyped samples. *Materials and Manufacturing Processes*, 15(1), 107–122.

Horvath, D., Noorani, R., & Mendelson, M. (2007). Improvement of surface roughness on ABS 400 polymer using design of experiments (DOE). *Materials Science Forum*, 561, 2389–2392.

Kristiawan, R. B., Imaduddin, F., Ariawan, D., Ubaidillah, & Arifin, Z. (2021). A review on the fused deposition modeling (FDM) 3D printing: Filament processing, materials, and printing parameters. *Open Engineering*, 11(1), 639–649.

Lužanin, O., & Plančak, M. (2014). Effect of layer thickness, deposition angle, and infill on maximum flexural force in FDM-built specimens. *Advanced Technologies and Materials*, 39(1), 49–58.

Mohamed, O. A., Masood, S. H., & Bhowmik, J. L. (2015). Optimization of fused deposition modeling process parameters: a review of current research and future prospects. *Advances in Manufacturing*, *3*, 42–53.

Nagarajan, V., Mohanty, A. K., & Misra, M. (2016). Perspective on Polylactic Acid (PLA) based Sustainable Materials for Durable Applications: Focus on Toughness and Heat Resistance. *ACS Sustainable Chemistry & Engineering*, 4(6), 2899–2916. doi: 10.1021/acssuschemeng.6b00321

Panda, S. K., Padhee, S., Anoop Kumar, S., & Mahapatra, S. S. (2009). Optimization of fused deposition modelling (FDM) process parameters using bacterial foraging technique. *Intelligent Information Management*, 1(02), 89.

Raut, S., Jatti, V. S., Khedkar, N. K., & Singh, T. P. (2014). Investigation of the effect of built orientation on mechanical properties and total cost of FDM parts. *Procedia Materials Science*, 6, 1625–1630.

Thrimurthulu, K., Pandey, P. M., & Reddy, N. V. (2004). Optimum part deposition orientation in fused deposition modeling. *International Journal of Machine Tools and Manufacture*, 44(6), 585–594.

Vasudevarao, B., Natarajan, D. P., Henderson, M., & Razdan, A. (2000). Sensitivity of RP surface finish to process parameter variation 251. *2000 International Solid Freeform Fabrication Symposium*.

Wu, W., Geng, P., Li, G., Zhao, D., Zhang, H., & Zhao, J. (2015). Influence of layer thickness and raster angle on the mechanical properties of 3D-printed PEEK and a comparative mechanical study between PEEK and ABS. *Materials*, 8(9), 5834–5846.

CHAPTER III

Fuel Cell Electrochemistry Measurement Methods

Nurettin ÇEK[1]
Ayhan ORHAN[2]
Selman SEZER[3]
İsmail DEMİR[4]

Introduction

The fuel cell is a type of galvanic cell that converts directly the chemical energy of the materials as fuel (e.g. hydrogen) into electrical energy. Electrical energy production of a fuel cell is associated with fuel and oxidizer supplies. In other words, as long as fuel and oxidant are provided the fuel cell produces electrical energy

[1*] PhD Student, Firat University, Institute of Science, Department of Metallurgical and Materials Engineering Technologies, Turkiye, nurettincek001@gmail.com
[2] Assoc. Prof. Dr., Firat University, Faculty of Technology, Department of Metallurgical and Materials Engineering, Turkiye
[3] Master Student, Firat University, Institute of Science, Department of Mechatronics Engineering, Turkiye
[4] Prof. Dr., Istanbul Ticaret University, Faculty of Engineering, Department of Mechatronics Engineering, Turkey, Chairman of the Board of Karabuk Iron and Steel Factories (KARDEMIR), Karabuk, Turkiye.

(Shah, 2007). Fuel cells are among clean and renewable energy sources (Çek 2016; Çek and Erensoy 2020).

The basic components of a fuel cell are anode electrode section (anodic catalyst layer) electrolyte, cathode electrode section (cathodic catalyst layer), and bipolar plates or interconnects. In addition, gaskets are sometimes used to seal or prevent gas leakage between the anode and cathode (Shah, 2007; Salvo et al. 2013). The components that make up the fuel cell are very important for fuel cell performance. Mechanical, chemical or thermal degradation occurs in these questionable components over time, and as a result, the performance of the fuel cell decreases (Çek and Sezer, 2023). Thus, taking into account that the durability of the materials is a very important factor, accurate calculation methods should be preferred.

Since fuel cells are a type of galvanic cell, they are electrochemical devices (Shah, 2007). For this reason, information about their performance is obtained by using various electrochemical measurement techniques (Lymperi et al. 2023). In scientific studies, electrochemical characteristics or analyzes of fuel cells are revealed using a device called potentiostat/galvanostat (Beltrán-Gastélum et al. 2023).

Measurements made using potentiostat/galvanostat device in studies on fuel cells are given below (Basu and Basu, 2011; Beltrán-Gastélum et al. 2023; Chen et al. 2014; Lymperi et al. 2023; Song et al. 2021):

- ✓ Open circuit voltage,
- ✓ Cyclic voltammetry or cyclic voltammogram,
- ✓ Linear voltammetry or linear voltammogram,
- ✓ Potentiodynamic polarization,
- ✓ Polarization curves and Chronopotentiometry,
- ✓ Electrochemical Impedance Spectroscopy.

The main purpose of is to raise awareness about the electrochemical characteristics of fuel cells by providing information about these measurement methods.

Open Circuit Voltage

The basic material of the thin catalyst layers present in the electrode sections of fuel cells is platinum that exists in nanometer size on carbon supports. Platinum, which is the important component of the catalyst layer, is a high-cost material. Catalyst losses occur due to various degradation processes in fuel cells. These processes occur in part under open circuit voltage (OCV) conditions of the fuel cell (Reimer et al. 2019).

OCV or OCP (Open Circuit Potential) is measured when the current value in the electrical circuit of an electrochemical cell equals zero. In other words, OCV is defined as the voltage value that occur at zero current in the electrical circuit of the electrochemical cell. OCV is closely related to the thermodynamic and kinetic performance of an electrochemical cell. The maximum electrical power that can be produced per unit current for a fuel cell is represented by OCV. In fuel cell operations the cell voltage is lower than the OCV value (Cammarata and Mastropasqua, 2023).

When no load is electrically connected to the fuel cells, the voltage produced is expressed as electromotive force (Çek, 2016; Çek and Erensoy 2020; Cammarata and Mastropasqua, 2023). This is the open circuit voltage of the fuel cell, which is mainly affected by the performance of the reactants (Gu et al. 2019).

It is often noted in fuel cell trials that the OCV value is not actually an unchanging number. The OCV value may vary depending on various single cells, manufacturer and operating circumstances (particularly humidification). Additionally, after switching to the OCV form, the cell voltage variations appear as a few mV for several hundred seconds, and timeless value is never seen. Under OCV condition, it is of great importance to understand the affects that occur on the catalyst surface in terms of degradation and long-term stability (Reimer et al. 2019).

Since OCV is observed when no current is being drawn from the fuel cell, it has important uses as follows (Cai, 2019):

- It is an important tool for the diagnosis of fuel cells,
- It allows accelerated life tests of fuel cells.

As long as the fuel cell operates, degradation occurs in the membrane. These degradations often occur from a combination of chemical, mechanical and thermal stressors. What is noteworthy here is that OCV plays a key role in chemical degradation. During OCV measurements of the fuel cell, it was observed that OCV performance decreased as the fuel cell membrane degraded (Zhao et al. 2020).

One of the areas where fuel cells are desired to be successfully implemented in daily life is automotive technologies. In the study conducted by Zhao et al. (2020), the following points were addressed for fuel cells to be successful in automotive applications.

- Fuel cell membrane must be resistant to OCV values greater than 0.8 V,
- They must have at least 5,000 hours of operation life including 30% idle time.

The OCV value of the fuel cell is affected by factors such as temperature, pressure and membrane humidity (Saleh et al. 2013; Zhao et al. 2020). In the study conducted by Saleh et al. (2013), the examination and analysis of the fuel cells' OCV values were presented under different operating temperatures and pressures and some of the results are given in Figure 1. The noteworthy part is that the OCV value is not constant and varies according to temperature and pressure.

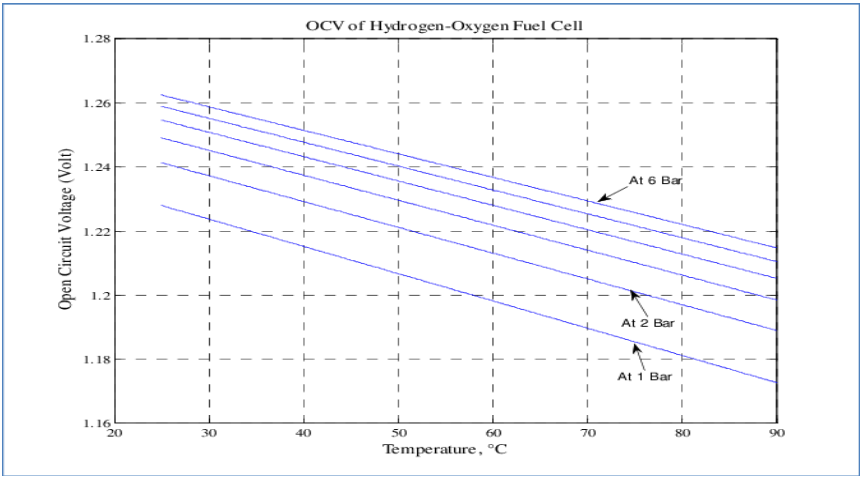

Figure 1. OCV values of a Hydrogen-Oxygen fuel cell at different pressures and temperatures (Saleh et al. 2013).

Cyclic Voltammetry

Thanks to the cyclic voltammetry (CV) technique, which is an electrochemical technique for the characterization of catalysts in the oxidation of fuels, it is possible to observe electrode surface behavior and to identify electrochemically active species. For this purpose, data is obtained by measuring the current flow after applying different potential values to the fuel cell (Muneeb, 2018).

It is used to examine changes in the total cathode active surface area in CV fuel cells. CV analysis tests are performed on the entire fuel cell stack with the potentiostat mode of the potentiostat/galvanostat device. The counter and reference electrodes of the potentiostat/galvanostat device are connected to the anode of the fuel cell. The working electrode is connected to the cathode of the fuel cell (Harel et al. 2011). The CV measurement method was carried out using a three-electrode cell. A three-electrode cell is generally used in CV measurements. This three-electrode cell consists of a counter electrode, reference and working electrodes. The counter electrode (CE) is important because the

current through the circuit also causes a reaction at the counter electrode. The working electrode (WE) has been noted as the heart of research, because what happens on the surface of this electrode is very important. The reference electrode (RE) is employed to minimize the effect of electrolyte resistance on the potential of the working electrode (Gouws, 2012).

The schematic representation of the three-electrode cell type CV measurement by Harel et al. (2011) is given in Figure 2.

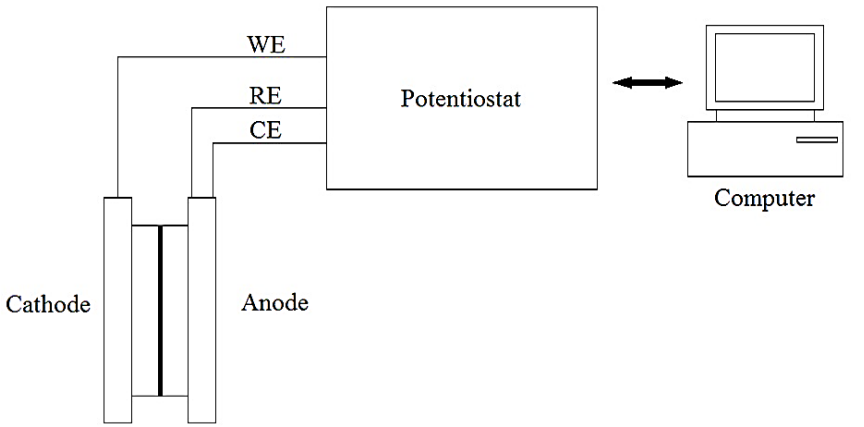

Figure 2. Schematic representation of the three-electrode cell type CV measurement (It was designed inspired by the study conducted by Harel et al (2011)).

In daily life applications, CV measurements of fuel cells are also measured using a two-electrode cell type. Most devices with a two-electrode cell type do not have an integrated reference electrode feature. The counter electrode is cleaned with hydrogen and simultaneously serves as the reference electrode (Internet 1). A schematic representation of the two-electrode cell type CV measurement is given in Figure 3.

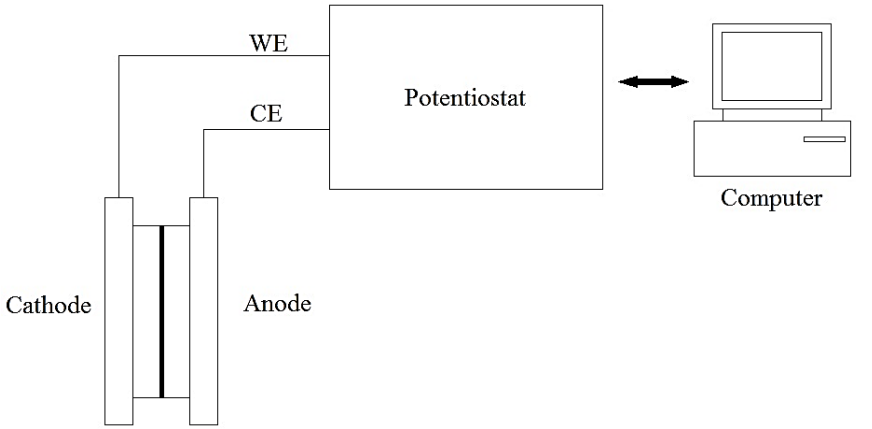

Figure 3. Schematic representation of the two-electrode cell type CV measurement (It was designed inspired by the study conducted by Internet 1).

Recently, the four-electrode cell type has also been used in CV measurements of fuel cells. In the four electrode cell types there are counter electrode (CE), working electrode (WE), reference electrode (RE), sense or RE (Ramani et al. 2017). The schematic representation of the four-electrode cell type CV measurement is given by Ramani et al. (2017) in Figure 4.

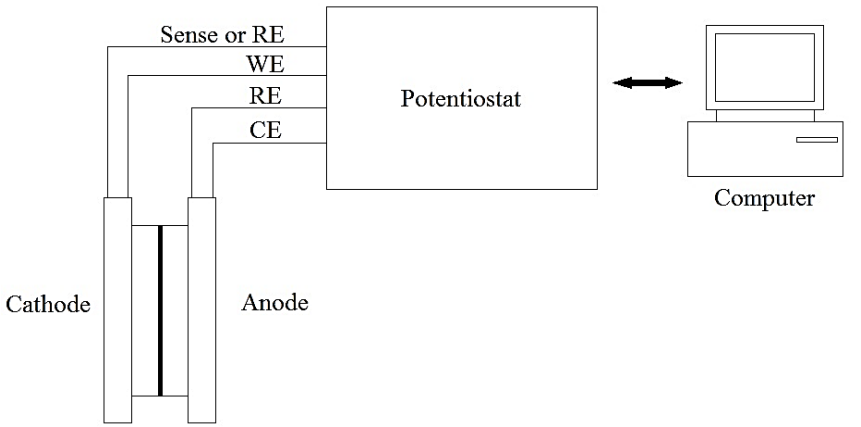

Figure 4. Schematic representation of the four-electrode cell type CV measurement (It was designed inspired by the study conducted by Ramani et al. (2017)).

As in many electrochemical cells, the oxygen reduction reaction (ORR), one of the basic reactions in fuel cells, is measured by CV or LSV (linear sweep voltammetry) methods (Gong, 2023). Moreover, information about the oxygen evolution reaction (OER) and hydrogen evolution reaction (HER) can also be provided by the CV technique. An example of CV analysis for a Pt electrode at room temperature, and alkaline conditions (pH 13.9) is given in Figure 5. As can be seen reversible peaks obtained from the adsorption-desorption processes of H_2, OH and O_2 on the Pt surface can be observed in the CV curve. In addition, the typical HER and OER reaction currents are clearly visible around -1000 and +1000 mV, respectively, against the Ag/AgCl reference electrode (Favaro et al. 2017).

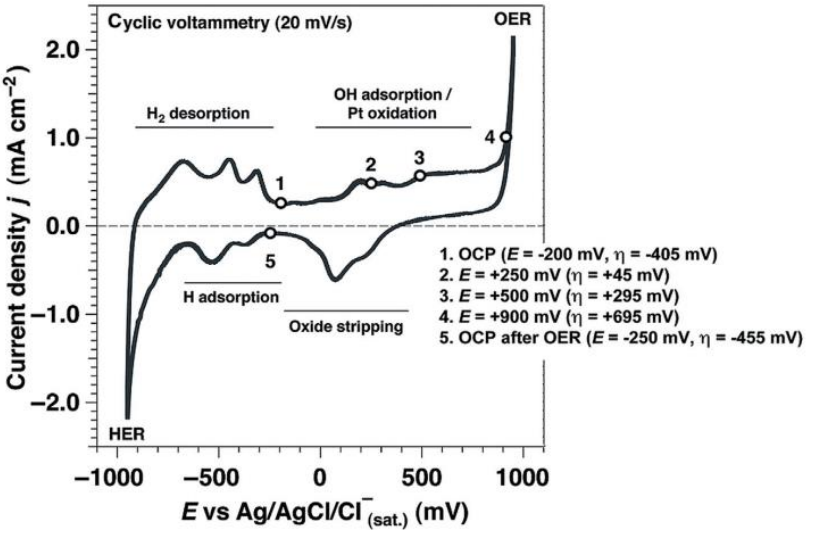

Figure 5. Example of cyclic voltammetry for a polycrystalline Pt electrode in alkaline conditions at room temperature (Favaro et al. 2017).

Linear Voltammetry

Linear sweep voltammetry (LSV) is a method that is a potentiostatic subset of basic cyclic voltammetry. In the LSV, the potential applied to the working electrode E is swept linearly between two points, initial voltage and final voltage, and the generated current is measured as a function of time. This property is different from CV. There are the situations where LSV is preferred over CV (Ahmad and Egilmez, 2022):

- Situations where the reaction is irreversible,
- Situations where useful information cannot be extracted from the return loop.

In other words, the entropy generated during a chemical reaction is large enough to make the process irreversible. LSV is a one-way and rapid technique compared to CV, providing both qualitative and quantitative analysis of an electrochemical system (Ahmad and Egilmez, 2022).

For LSV measurement, the connections of the potentiostat device and the fuel cell are the same as the CV technique. In a fuel cell study, a three-electrode cell type was established for LSV measurement, and hydrogen flowed from the counter/reference electrode and humidified nitrogen flowed from the WE. Voltage was swept from 0.05 V to 0.5 V at a scan rate of 1 mV s^{-1} for linear sweep voltammetry. Thus, LSV measurement was carried out and an example measurement graph is given in Figure 6 (Baricci and Casalegno, 2023).

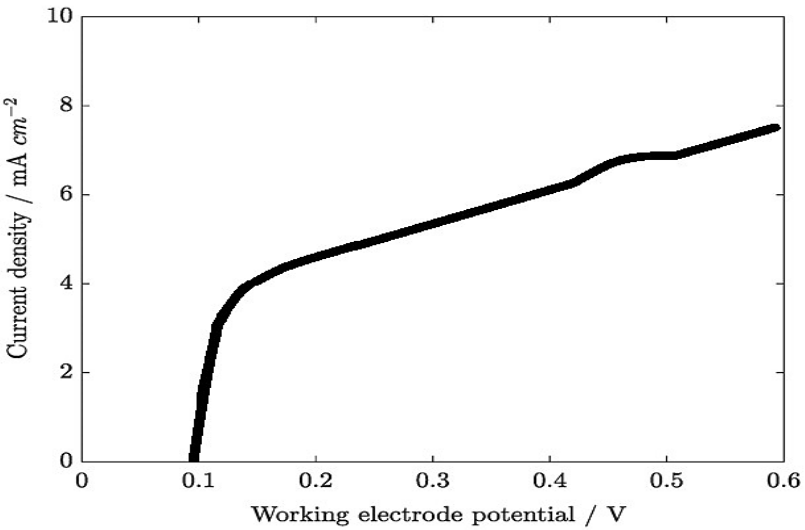

Figure 6. LSV graph of a sample study (It was designed inspired by the study conducted by Baricci and Casalegno, (2023)).

Potentiodynamic Polarization

Potentiodynamic polarization tests are a type of electrochemical testing (Zhang et al. 2020). A three-electrode cell type electrochemical cell is used to perform these tests. The electrochemical cell is also called a three-electrode corrosion cell. The electrochemical cell in question consists of a WE, CE and a RE

(Heo and Kim, 2023). Especially, in recent studies (Zhang et al. 2020; Heo and Kim 2023), potentiodynamic tests have been performed using a three-electrode cell type system.

In the study by Zhang et al. (2020), a traditional three-electrode system was used in the electrochemical test. A saturated calomel electrode (SCE) was used as the reference electrode, a platinum plate as the counter electrode, and a ZnC-coated Ti plate as the working electrode. In order to simulate the operating environment of the proton exchange membrane fuel cell (PEMFC), 0.05 mol/L H_2SO_4 solution and 2 ppm HF solution were used as corrosion solutions and tested at approximately 70 °C in the electrochemical test. The exposed area of the sample used for electrochemical testing was 10 mm×10 mm. The sample (working electrode) was cleaned with acetone through ultrasonic cleaner before testing. A simulated PEMFC cathodic environment (0.6 VSCE, air purged) and anodic environment (-0.1 VSCE, H_2 purged) were set during the testing of the potentiodynamic polarization curve. The results of the potentiodynamic tests of the study in question are as follows (Zhang et al. 2020):

- The corrosion potential of the ZrC-coated Ti plate increases significantly compared to pure Ti in both cathodic and anodic environments.
- Basically, higher corrosion potential means better corrosion resistance and inertness.
- The corrosion current density of the ZrC-coated Ti sheet was reduced by about two times, which shows that the corrosion resistance of the Ti sheet can be significantly increased by ZrC coating.
- Compared to the bare Ti plate, the modified sample exhibits a corrosion current density approximately two orders of magnitude lower in both cathodic and anodic environments.
- It is obvious that the ZrC-coated Ti sheet has better corrosion resistance in the PEMFC environment.

In the study by Heo and Kim (2023), potentiodynamic polarization for PEMFC tests were performed with a scan rate of 1.0 mV/s in the potential range from −0.25 V to +1.6 V relative to the open OCP. Corrosion potential (E_{corr}) and corrosion current density (I_{corr}) were calculated using the Tafel extrapolation method in the range of ±0.25 V based on the OCP of the potentiodynamic polarization curves. In the potentiodynamic polarization experiment, no active peak in current density was observed in the TiN-coated sample due to corrosion in the anode or cathode environments. The corrosion current density was found to be less than 1 μA/cm^2.

Potentiodynamic analysis results help provide information about the porosity of the material attached to the working electrode. To calculate porosity, E_{corr}, I_{corr} and Tafel slope (βa, βc) values are calculated using the Tafel extrapolation method from the potentiodynamic polarization curve. The results were calculated using Equations (1) and (2), and represent polarization resistance (R_p) and porosity (P), respectively (Heo and Kim, 2023). The graphical results are shown in Figure 7.

$$R_p = \frac{\beta a \; x \; \beta c}{2{,}303 \; x \; I_{corr} \; x \; (\beta a + \beta c)} \quad (1)$$

$$P = (R_{ps}/R_p) \text{ x } 10^{-[\triangle Ecorr]/\beta a} \quad (2)$$

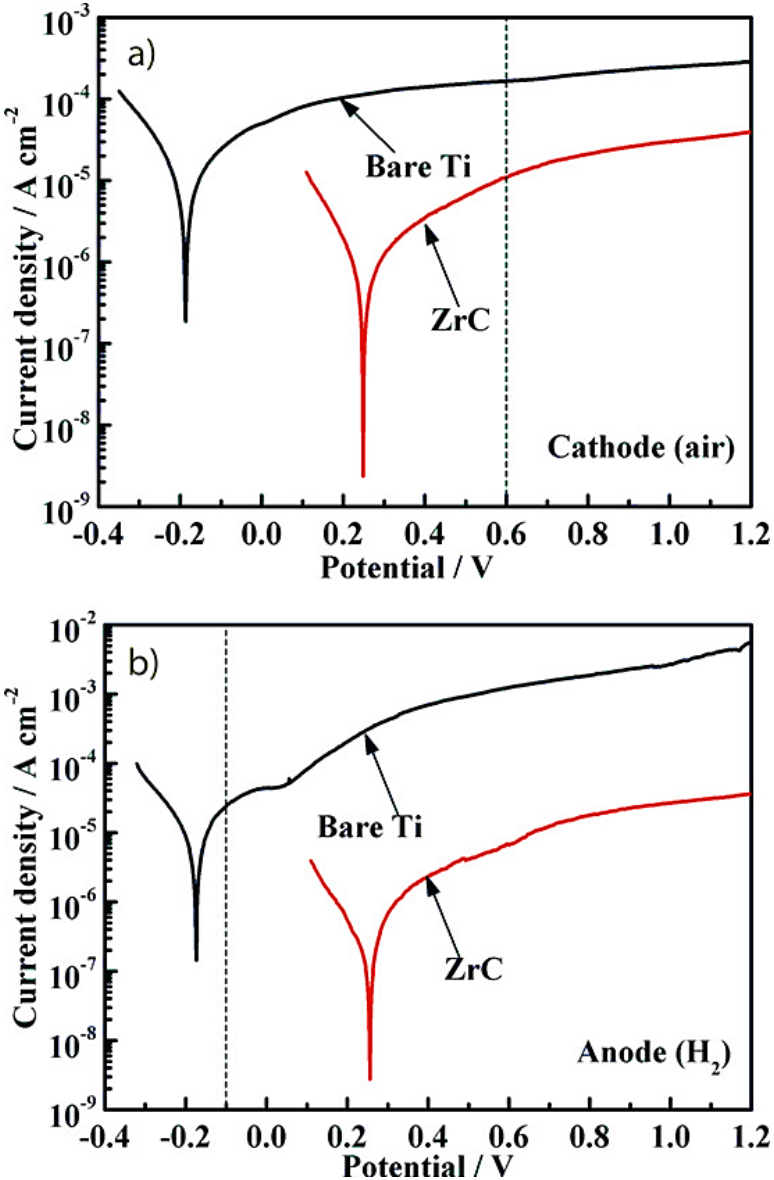

Figure 7. Potentiodynamic polarization curves for ZrC-coated Ti and bare Ti bipolar plate in simulated (a) cathodic and (b) anodic media (Zhang et al. (2020)).

Polarization Curves and Chronopotentiometry

Polarization curves are used to determine the performance of the fuel cell. Thes curves define the relationship between the output voltage and current density in fuel cells, and it is stated as the most important characteristic property (Hao et al. 2016).

The polarization curves of the fuel cell are revealed by a classical three-electrode electrochemical cell technique using a potentiostat (Lamy et al. 2020). The connections of the mentioned three-electrode electrochemical cell system are the same as the three-electrode cell type in the CV method. In order to generate polarization curves of fuel cells accurately, OCV values must be stable.

In recent studies (Carvela et al. 2021; Islam et al. 2022) on fuel cells, polarization curves of fuel cells were determined in potentiostatic mode using a potentiostat/galvanostat device.

In another study by Islam et al. (2022), the fuel cell was connected to a potentiostat/galvanostat device. For operation as a fuel cell, all experiments were carried out in potentiostatic mode (0.5V constant voltage) and atmospheric pressure for 20 minutes.

Chronopotentiometry is applied between the working and the counter electrodes. It is promoted as a current step technique. Chronopotentiometry analysis is an effective electrochemical characterization method to examine the ability of a fuel cell containing a membrane electrode assembly (MEA) to provide the correct voltage response for a given fuel cell current. It provides information about the best operating conditions of fuel cell relating to different parameters such as relative humidity, operating pressure, cell temperature, etc. Chronopotentiometry of the fuel cell is measured in galvanostatic mode (current step) to measure the voltage of the cell (Ahmad and Egilmez, 2021).

Polarization curves are obtained mostly galvanostatically. In other words, a constant current is drawn from the fuel cell and the voltage response is measured. An important feature of the

polarization curve is the open circuit voltage, which is the cell voltage without any electrical charge (Internet, 2).

Although there are various methods for generating fuel cell polarization curves, they all end up in similar shapes. For example, a typical polarization curve for a PEM fuel cell is shown in Figure 8. As can be seen here, performance losses of the fuel cell can also be detected by the polarization curves. Performance losses generally present in fuel cells are activation losses, ohmic losses and concentration losses (Du et al. 2021).

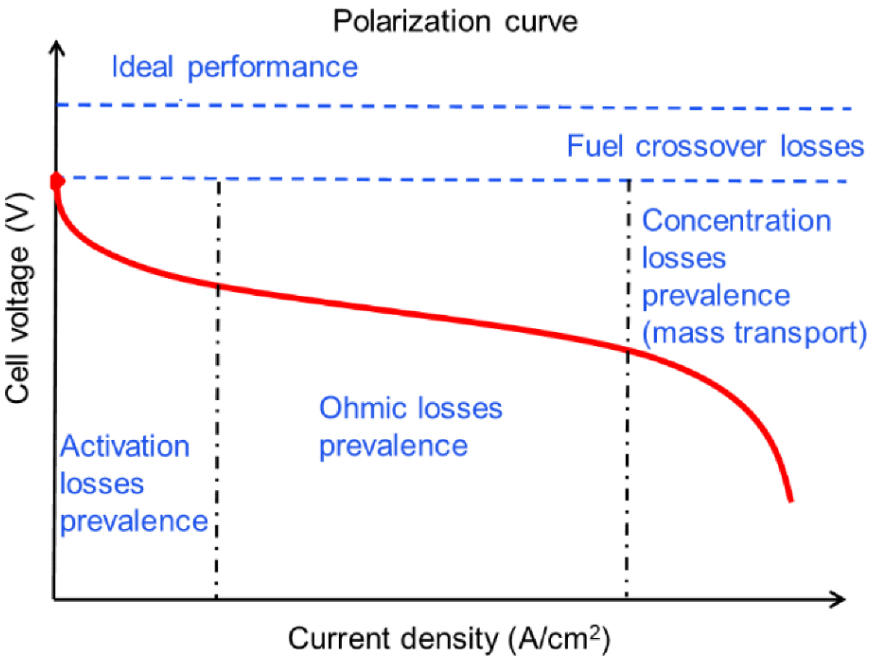

Figure 8. Classic polarization curve for PEM fuel cells (Du et al. 2021).

Power/power density values are found by multiplying the voltage and current/current density values obtained in the polarization curves and then power curves are generated (O'Hayre, 2017). Figure 9 presents an example type of graph showing the polarization and power curves of fuel cells together.

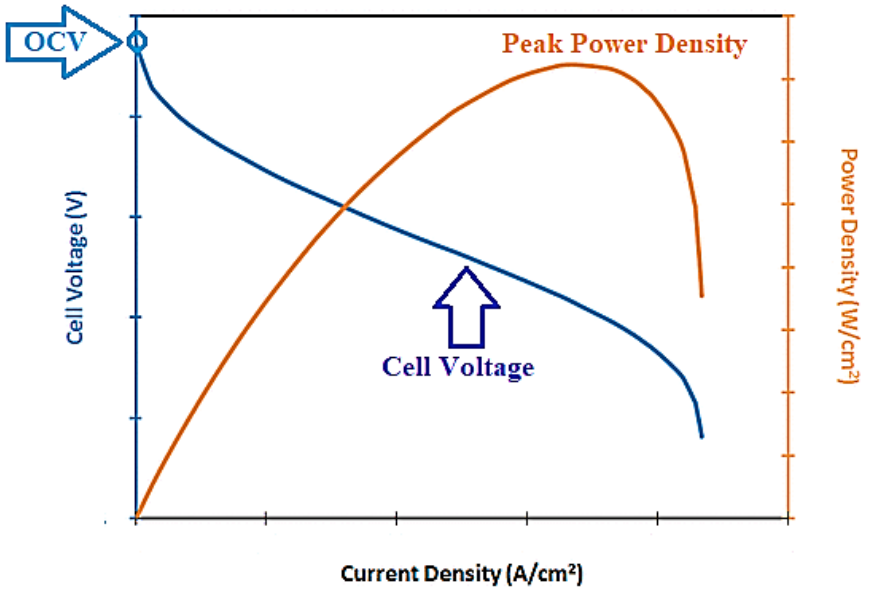

Figure 9. Display of polarization and power curves of fuel cells on the same graph It was designed inspired by the study conducted by O'Hayre, (2017)).

Electrochemical Impedance Spectroscopy

Electrochemical impedance spectroscopy (EIS) exercises are performed by establishing a two-electrode electrochemical cell system or a three-electrode electrochemical cell system (Padha et al. 2022).

EIS studies of electrochemical devices (for example fuel cells and batteries) are generally performed by generating a two-electrode electrochemical cell type. In addition, EIS measurements can also be made by generation of an electrochemical cell type with three or four electrodes (Lazanas and Prodromidis, 2023).

When EIS measurements of fuel cells are generated by using the two-electrode electrochemical cell type, but a reference electrode is not used (Nakajima, 2011).

Figure 10 shows the setup of a fuel cell for EIS measurement for a two-electrode electrochemical cell type. For EIS measurements based on the usage of the two-electrode electrochemical cell type, the anode of the fuel cell is fed with hydrogen while the cathode is fed with oxygen. The counter electrode (CE) of the potentiostat/galvanostat device is connected to the fuel cell anode, and the working electrode (WE) is connected to the fuel cell cathode (Nakajima, 2011; Braz et al. 2022).

Three-electrode electrochemical cell type for EIS measurements includes the WE, the CE, and the RE (Braz, et al. 2022). Figure 11 shows the setup of a fuel cell for EIS measurement using a three-electrode electrochemical cell type.

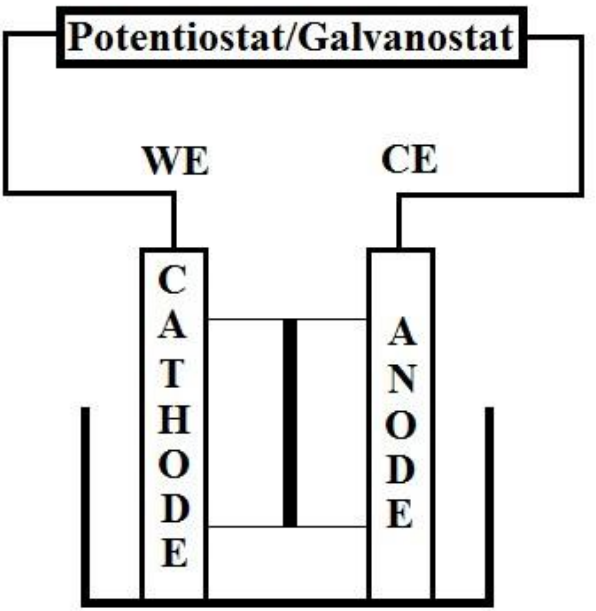

Figure 10. Schematic representation of the two-electrode cell type for EIS measurement (It was designed inspired by the study conducted by Nakajima, (2011); Braz et al. (2022)).

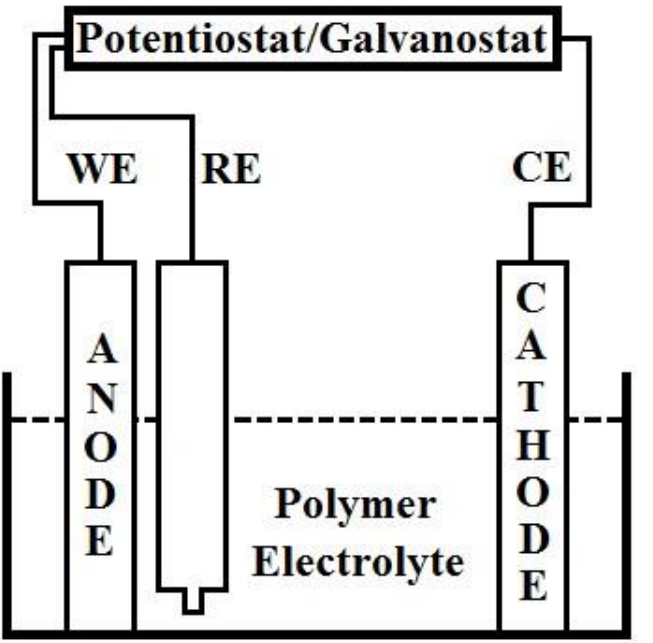

Figure 11. EIS measurement setup of a PEM fuel cell using a three-electrode electrochemical cell type (It was designed inspired by the study conducted by Yuan et al. (2007)).

EIS is a non-destructive, convenient and powerful testing method for fuel cells testing. EIS does not destabilize the fuel cell system and provides handy info touching fuel cell performance and components. The essential benefit of EIS is the dexterity to distinguish individual contributions of interfacial charge transfer and mass transfer resistances in the catalyst and diffusion layers. The weakness of EIS analysis is that it does not produce local knowledge (Asghari et al. 2010).

In EIS tests, the Nyquist and the Bode plots are generated generally. Nyquist plot provides information about the correlation

among the real and imaginary regions of impedance whenever the frequency changes. The weakest aspect of the Nyquist plot is that frequency knowledge cannot be displayed directly. Bode plot supplies knowledge touching magnitude and phase angle. That is, the Bode plot ensures knowledge regarding how the magnitude and phase angle of the impedance change as a function of frequency, respectively (Huang et al. 2016).

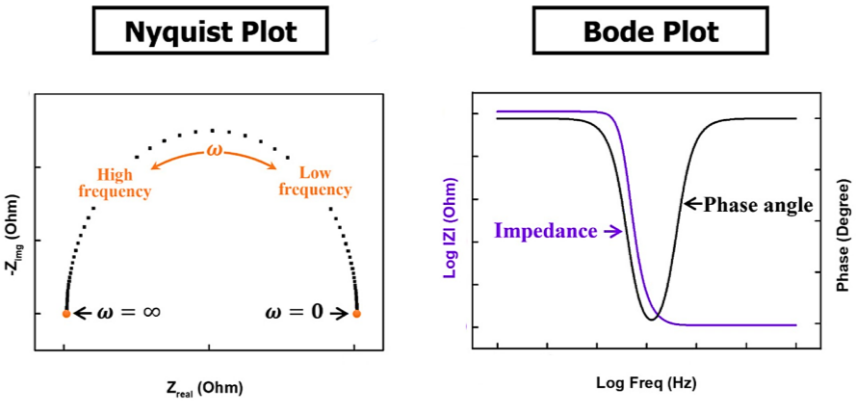

Figure 12. A representative show of Nyquist and Bode charts in EIS tests (It was designed inspired by the study conducted by Internet 3).

References

Ahmad, S. and Egilmez M. (2021). Battery testing methods in fuel cell research. *Condensed Matter Materials Science*, arXiv:2209.14541.

Asghari, S., Mokmeli, A., Samavati, M. (2010). Study of PEM fuel cell performance by electrochemical impedance spectroscopy. *International Journal of Hydrogen Energy,* 35, (17), 9283-9290.

Basu, D. and Basu, S. (2011). Synthesis and characterization of Pt–Au/C catalyst for glucose electro-oxidation for the application in direct glucose fuel cell. *International Journal of Hydrogen Energy* 36, (22), 14923-14929.

Braz, B.A., Moreira, C.S., Oliveira, V.B., Pinto, A.M.F.R. (2022). Electrochemical impedance spectroscopy as a diagnostic tool for passive direct methanol fuel cells. *Energy Reports*, 8, 7964-7975.

Baricci, A. and Casalegno, A. (2023). Experimental Analysis of Catalyst Layer Operation in a High-Temperature Proton Exchange Membrane Fuel Cell by Electrochemical Impedance Spectroscopy. *Energies,* 16, (12), 4671.

Beltrán-Gastélum, M., Portillo-Fuentes, S.G., Flores-Hernández, J.R., Salazar-Gastélum, M.I., Trujillo-Navarrete, B., Romero-Castañón, T., Silva-Carrillo, C., Reynoso-Soto, E.A., Félix-Navarro, R.M. (2023). Ag-Cu Nanoparticles as Cathodic Catalysts for an Anion Exchange Membrane Fuel Cell. *Catalysts*, 13 (7), 1050.

Cai, Y. (2019). The Open Circuit Voltage of Polymer Electrolyte Membrane Fuel Cells. Doctoral thesis, Rheinisch-Westfälischen Technischen Hochschule Aachen, Germany.

Cammarata, A. and Mastropasqua, L. (2023). Theoretical analysis of mixed open-circuit potential for high temperature electrochemical cells electrodes. *Front. Energy Res.*, 11, 1120343.

Carvela, M., Lobato, J., Rodrigo, M.A. (2021). Chloralkali low temperature PEM reversible electrochemical cells. *Electrochimica Acta*, 387, 138542.

Chen, P., Wu, H., Yuan, T., Zou, Z., Zhang, H., Zheng, J., Yang, H. (2014). Electronspun nanofiber network anode for a passive direct methanol fuel cell. *Journal of Power Sources*, 255, 70-75.

Çek, N. (2016). Parçacıklar ve Enerji Kaynakları. Saarbrucken, Lambert Academic Publishing.

Çek, N. and Erensoy, A. (2020). Yakıt Hücresi Teknolojilerinde Gelişmeler. Ankara, Nobel Academic Publishing.

Çek, N. and Sezer, S. (2023). Fuel Cells Applications, Materials and Power Management Circuits. In: *Research Trends in Multidisciplinary Research* (Volume - 44), India, AkiNik Publications.

Du, L., Zhang, G., Sun, S. (2021). Proton Exchange Membrane (PEM) Fuel Cells with Platinum Group Metal (PGM)-Free Cathode. *Automotive Innovation*, 4, 131-143.

Favaro, M., Valero-Vidal, M., Eichhorn, J., Toma, F.M., Ross, P.N., Yano, J., Liu, Z., Crumlin, E.J. (2017). Elucidating the alkaline oxygen evolution reaction mechanism on platinum. J. Mater. Chem. A, 2017, 5, 11634-11643.

Gu, J., Wang, C., Zhao, N. (2019). Modeling and Simulation of the Electrical Characteristic of Solid Oxide Fuel Cells. *IOP Conf. Series: Journal of Physics: Conf. Series*, 1314, 012062.

Gong M. (2023). Case Study on the Reproducibility of Characterizing the Electrocatalytic Activity of $La_{1-x}Sr_xMnO_3$ in ORR. *Crystals*, 13, (1), 74.

Gouws, S. (2012). Voltammetric Characterization Methods for the PEM Evaluation of Catalysts. In: Kleperis, J. (Eds) Electrolysis, InTech.

Harel, F., Bégot, S., Wasterlain, S., Candusso, D. (2011). Electrochemical characterisation of fuel cell stack during cold start. *The European Physical Journal - Applied Physics,* 44, 2, 23402.

Hao, D., Shen, J., Hou, Y., Zhou, Y., Wang, H. (2016). An Improved Empirical Fuel Cell Polarization Curve Model Based on Review Analysis. *International Journal of Chemical Engineering,* 2016, 4109204.

Heo, H-S. and Kim, S-J. (2023). Investigation of Electrochemical Characteristics and Interfacial Contact Resistance of TiN-Coated Titanium as Bipolar Plate in Polymer Electrolyte Membrane Fuel Cell. *Coatings,* 13(1), 123.

Huang, J., Li, Z., Liaw, B.Y., Zhang, J. (2016). Graphical analysis of electrochemical impedance spectroscopy data in Bode and Nyquist representations. *Journal of Power Sources,* 309, 82-98.

Internet 1. https://www.horiba-fuelcon.com/en/truedata-cyv-cyclic-voltametry (3.10.2023).

Internet 2. https://www.hi-ern.de/en/research/electrocatalytic-interface-engineering-1/composite-membrane-analysis-and-design/electrochemical-characterization (6.10.2023).

Internet 3.https://wiki.aalto.fi/display/SSC/Electrochemical+impedance+spectroscopy (8.10.2023).

Islam, M.N., Mansoor Basha, A.B., Kollath, V.O., Soleymani, A.P., Jankovic, J., Karan, K. (2022). Designing fuel cell catalyst support for superior catalytic activity and low mass-transport resistance. *Nature Communications,* 13, 6157.

Lamy, C., Coutanceau, C., Baranton, S. (2020). Chapter three - Experimental part. In: Lamy, C., Coutanceau, C., Baranton, S. (eds) In Hydrogen and Fuel Cells Primers, Production of Clean Hydrogen by Electrochemical Reforming of Oxygenated Organic Compounds. Academic Press.

Lazanas, A.C. and Prodromidis, M. I. (2023). Electrochemical Impedance Spectroscopy─A Tutorial. *ACS Measurement Science* Au, 3, 3, 162-193.

Lymperi, A., Chatzilias, C., Xydas, F., Martino, E., Kyriakou, G., Katsaounis, A. (2023). Electrochemical Promotion of CO_2 Hydrogenation Using a Pt/YSZ Fuel Cell Type Reactor. *Nanomaterials,* 13,

Muneeb, O. (2018). Catalysts for Electrochemical Oxidation of Renewable Fuels. *Master of Science Thesis*. California State University, Fullerton.

Nakajima, H. (2011). Electrochemical Impedance Spectroscopy Study of the Mass Transfer in an Anode-Supported Microtubular Solid Oxide Fuel Cell. In: Nakajima, H. (eds) *Mass Transfer - Advanced Aspects*. InTech.

O'Hayre, R.P. (2017). Fuel cells for electrochemical energy conversion. *EPJ Web of Conferences,* 148, 00013.

Padha, B., Verma, S., Mahajan, P., Arya, S. (2022). Electrochemical Impedance Spectroscopy (EIS) Performance Analysis and Challenges in Fuel Cell Applications. *J. Electrochem. Sci. Technol.*,13(2), 167-176.

Ramani, V.K., Cooper, K., Fenton, J.M., Kunz, H.R. (2017). Polymer Electrolyte Fuel Cells. In: Breitkopf, C., Swider-Lyons, K. (eds) *Springer Handbook of Electrochemical Energy*. Springer Handbooks. Springer, Berlin, Heidelberg.

Reimer, U., Cai, Y., Li, R., Froning, D., Lehnert, W. (2019). Time Dependence of the Open Circuit Potential of Platinum Disk Electrodes in Half Cell Experiments. *Journal of The Electrochemical Society*, 166(7), F3098-F3104.

Salvo, M., Casalegno, V., Rizzo, S., Smeacetto, F., Ventrella, A., Ferraris, M. (2013). Glasses and glass-ceramics as brazing materials for high-temperature applications. Advances in Brazing

Science, Technology and Applications, Woodhead Publishing Series in *Welding and Other Joining Technologies*, pp. 525-544.

Saleh, I.M.M., Calay, R.K., Rashid, A. (2013). Modelling and Examining Open Circuit Voltage for PEM Fuel Cells. *Journal of Electrical Engineering,* 13(3), 140-146.

Shah, R.K. (2007). Introduction to Fuel Cells. In: Basu, S. (eds) *Recent Trends in Fuel Cell Science and Technology*. New York, Springer.

Song, H-B., Park, J-H., Park, J-S., Kang, M-S. (2021). Pore-Filled Proton-Exchange Membranes with Fluorinated Moiety for Fuel Cell Application. *Energies*, 14(15), 4433.

Yuan, X., Wang, H., Sun, J. C., Zhang, J. (2007). AC impedance technique in PEM fuel cell diagnosis—A review. *International Journal of Hydrogen Energy,* 32, (17), 4365-4380.

Zhang, P.C., Han, Y.T., Shi, J.F., Li, T., Wang, H.Y., Wang, X.Y., Sun, J.C. (2020). ZrC Coating Modified Ti Bipolar Plate for Proton Exchange Membrane Fuel Cell. *Fuel Cells – From Fundamentals to Systems,* 20, (5), 540-546.

Zhao, N., Chu, Y., Xie, Z., Eggen, F., Girard, F., Shi, Z. (2020). Effects of Fuel Cell Operating Conditions on Proton Exchange Membrane Durability at Open-Circuit Voltage. *Fuel Cells – From Fundamentals to Systems,* 20, (2), 176-184.

CHAPTER IV

Comparisons of fatigue crack growth rates for particulate reinforcement composite and base alloy

Ilyas UYGUR[1]

Introduction

Metal matrix composites (MMCs) are materials composed of a metallic matrix and one or more secondary phases, such as ceramic, metallic, or organic reinforcements. MMCs offer improved properties such as high strength, stiffness, wear resistance, and thermal conductivity compared to monolithic metals due to the addition of the reinforcement phase. MMCs find applications in aerospace, automotive, and electronics industries due to their lightweight, high-performance properties. Common types of MMCs include aluminum matrix composites, titanium matrix composites,

[1] * Prof. Dr. Duzce University, Faculty of Engineering, Department of Mechanical Engineering, Turkiye, ilyasuygur@duzce.edu.tr. ORCID.0000-0002-8744-5082.

and magnesium matrix composites. Particulate reinforced composites are composite materials consisting of a metal matrix and small, reinforcing particles, typically ceramic or metallic. The addition of these particles can significantly improve the mechanical properties of the composite, such as strength, stiffness, and wear resistance. The combination of 2000 series aluminum alloys with particulate reinforcements can result in high-performance materials that have superior properties compared to traditional aluminum alloys. These composites can be used in applications such as engine components, automotive parts, and sporting equipment. However, their production and processing require specialized techniques due to the difficulty in uniformly dispersing the reinforcing particles within the aluminum matrix (Uygur, 1999).

The fatigue response of Al-based composites has received reasonable attention in the literature. The tensile responses (Uygur, 2004), High Cycle Fatigue properties (Uygur et al., 2004), Low Cycle Fatigue properties (Uygur and Kulekci, 2002), Notch behaviour, and fatigue life predictions (Uygur,2011, Uygur et al. 2014) and fatigue crack propagation response (Bache et al. 2000, Uygur, 2024) of Al-SiCp composites have been extensively investigated. The fatigue response of MMCs has been influenced by several factors, including the type of matrix alloy, type of reinforcement (continuous, whisker, or particle), composition of reinforcement, heat treatment, processing methods, and volume fraction (Vf) and size of reinforcement (Pz) (Uygur, 1999). Unfortunately, the presence of hard and brittle ceramic reinforcements reduces the monotonic ductility, fatigue crack growth resistance at high growth rates, and fracture toughness compared with the monolithic Al-alloy. These properties are crucial for component reliability and design in many industrial applications. It is important to appreciate that there is always the possibility that complex and highly stressed structures can contain flaws. The useful life in such situations will depend on the rate of crack propagation from these inherent flaws to a critical size for catastrophic failure. Many failures of structural parts in service occur under various

loading and environmental conditions, where the characteristics of reinforcements may change the fatigue crack growth rates and crack initiation of the composites. Although the tensile and some fatigue of these composites have been studied widely (Uygur, 1999, 2004, 2002, 2011, 2014, 2024), the information available on their fatigue crack propagation is limited. In general, the role of the reinforcement particles is well understood in many studies, but there are limited literature comparisons on the fatigue crack propagation rates of the base alloy and its composite. Thus, this particular research is mainly aimed at investigating the effect of materials on the fatigue response of the 2124/SiCp composite and its base alloy in naturally aged (T4) conditions.

Materials and Experimental procedures.

The materials used in this study were commercially available 2124 (Al-Cu-Mg-Mn) Al-alloys with 25 vol% SiCp MMCs. These materials were produced by Aerospace Composite Materials (U.K.), labeled as AMC225 (25vol% 2-3 μm SiCp) and AMC200 for the base alloy, using PM processing. Prior to the machining process, a solution treatment was applied at 505 oC for 1 h, followed by cold water quenching, and then natural aging (T4) at room temperature. The alloy composition, particle size detection and distribution, and tensile response of these composites were extensively investigated and discussed elsewhere (Uygur, 2004).

For the fatigue crack propagation evaluation, a 5x5 mm 'Corner Crack' (CC5) test piece design was adopted, as shown in Figure 1, where probe wire positions for the DC Potential Drop (PD) are also shown in the same figure. A crack was initiated from an edge slit 0.25 mm deep. Pulsed Direct Current (DC) potential drop systems were used to monitor crack growth. At predetermined stages of the test, a constant DC power supply delivered a 50 A, two-pulse to the specimen for 2 s, while the fatigue cycles were held at 75% of the peak load. During this period, the potential drop was measured across the crack. Potential drop data were converted to length, and Fatigue Crack Growth Rates (FCGR) were assessed as a function of

applied Stress Intensity Range ΔK (Lu, 1999). Calibration trials and comparisons with data obtained using optical and DC potential drop systems have established that the pulsed DC system has no measurable effect on the rate of crack propagation in these materials. DC PD monitoring was carried out using 0.3 mm diameter insulated probe wires, which were attached to the specimen by means of a 50-watt spot weld (Hughes Aircraft Company). The welding current was set at 2-2.5 A. The effects of cyclic frequency (55 Hz), R ratio R=0.1 and R=0.5, and 1 Hz sine wave form were applied to all samples. All tests were performed under constant amplitude load control testing conditions in various servo-hydraulic machines. Fatigue crack growth rate tests were performed in air and 3.5% salt solution environments.

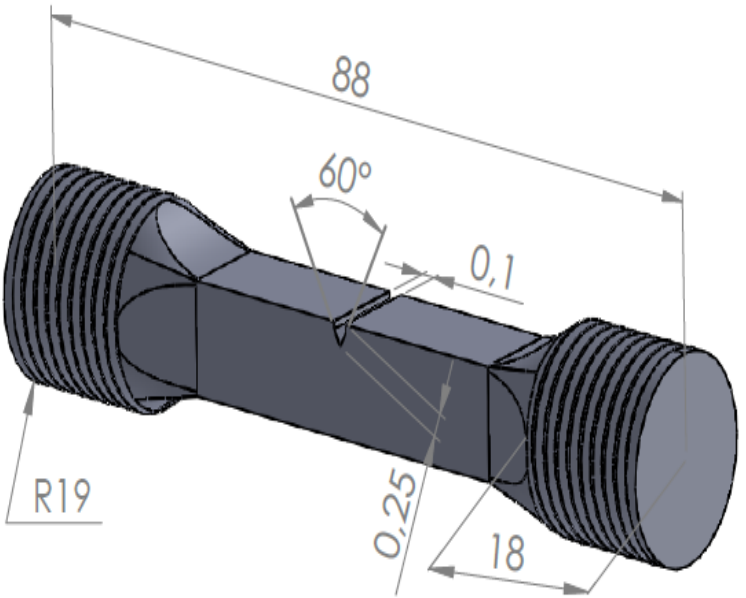

Figure 1. Fatigue crack propagation test sample CC5

Results and Discussions

The room temperature Fatigue Crack Growth Rates (FCGR) for AMC 225 MMC and AMC200 base alloy are compared at a stress ratio of 0.1 in Figure 2. The increase in the applied maximum stress from 150 to 175 MPa caused slightly faster crack growth at low ΔK. The very early crack growth rate for the test conducted at 150 MPa was relatively high, immediately followed by a marked period of retardation during which the crack virtually arrested at ΔK = 5 MPa√m. Subsequent loading forced the crack growth to advance once more. This type of behaviour is characteristic of small cracks. The absence of reinforced SiC particles in the base alloy is associated with an enhanced crack growth rate level for 2124 base alloy and 7017 Al-alloy in air at R=0.1 (Lu, 1999). The crack growth rates of the unreinforced base alloy are significantly higher, and the apparent ΔKth value lower than that of the composite. The difference can be explained by roughness-induced crack closure. Two main factors trigger firstly, nano-scale roughness on the crack surface, secondly degree of deflection (micro-roughness). These factors affect the friction stress acting on the crack planes and the stress intensity factor range for crack closure (Mizoguchi et al., 2018). The higher yield and elastic modulus of the composite, compared to the monolithic alloy, reduces the cyclic crack tip opening distance so that the fracture surface in the crack wake contacts earlier in the composite.

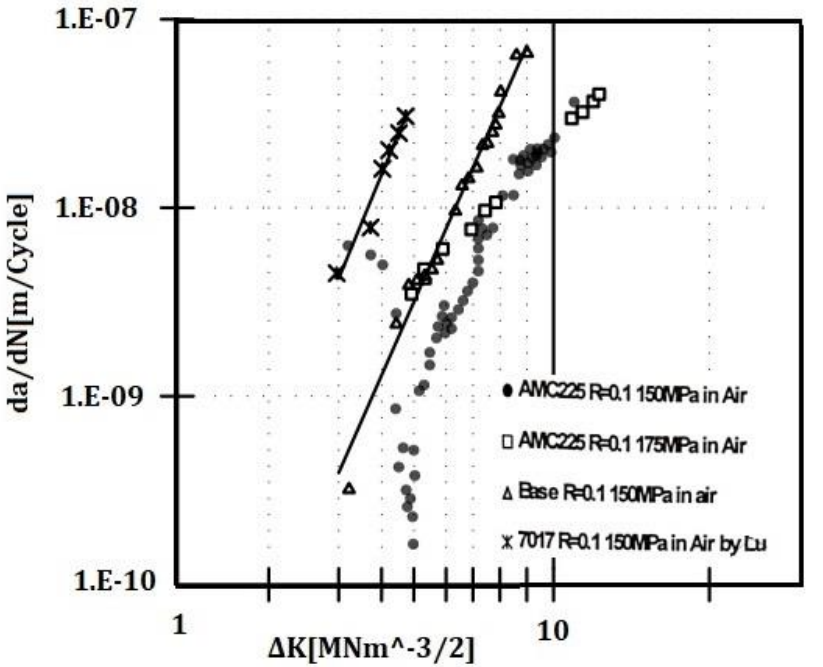

Fig.2. Comparison of FCGR for AMC 225, unreinforced base AMC200 and 7017 Al-alloy at R=0.1 in air.

Figure 3 compares long crack growth data obtained at R=0.5 in air for the MMC and the base alloy. The base material FCGR is slightly lower than that of the composite material, therefore, it can be argued that the benefit of the reinforcement particles has disappeared at high R ratios. Once again, the FCGR of 7017 Al-alloy is extremely high relative to the 2000 series Al-alloy and composite. At high R values, the crack closure effects are minimal, and FCGR are only slightly lower in the base alloy than in the composite. This behavior may also be related to the high fracture toughness of the base alloy compared to the composite.

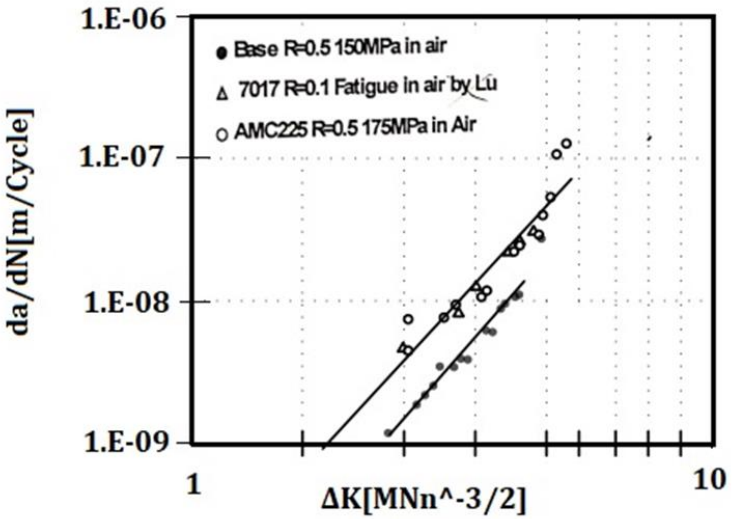

Fig.3. Comparisons of FCGR for AMC 225, unreinforced base AMC200 and 7017 Al-alloy at R=0.5 in air.

The FCGR in salt solution are plotted in Figures 4 and 5 for 2124 MMC and 7017 alloys at R=0.1 and R=0.5, respectively. It is evident that the crack growth rates are similar for the MMC and the base alloy in a salt solution. The beneficial effect of reinforcement at low R ratio (R=0.1) in air is not observed in the salt solution environment. These observations may be attributed to enhanced Hydrogen Embrittlement (HE) in materials where the crack tip is always open, and the fracture surfaces are extensively exposed to the hostile environment. The HE fracture mechanism may be the governing process in both base and composite FCGR in a salt solution environment. Again, very high crack growth rates were observed in the 7017 Al-alloy at R=0.1 for the salt solution, where FCGR are as fast as the R=0.5 crack growth response of the MMC material. Hydrogen embrittlement (HE) represents the deterioration of the mechanical properties of metals or alloys due to the presence of dissolved hydrogen in the lattice (Djukic et al., 2019). The HE

usually results in the loss of ductility, the decrease of fracture toughness, the increase in fatigue fracture growth rate (FCGR), and brittle fracture failure in steel at low or subcritical stress levels (Lee et al., 2023).

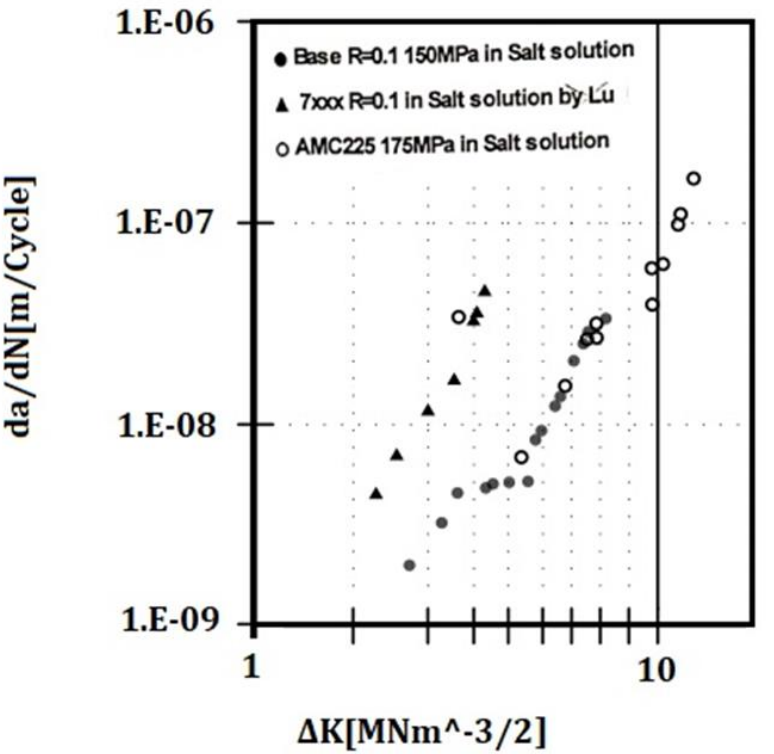

Fig.4. Variations on FCGR for AMC 225, unreinforced base AMC200 and 7017 al-alloy at R=0.1 in salt solution.

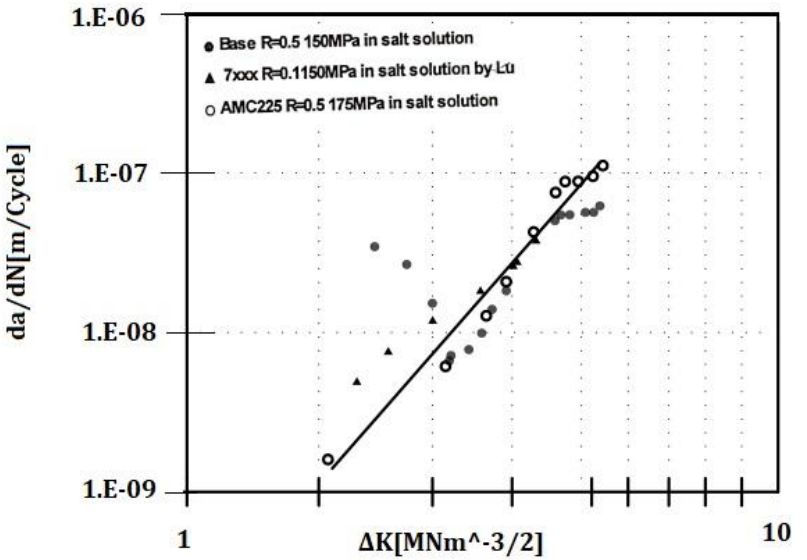

Fig.5. Variations on FCGR for AMC 225, unreinforced base AMC200 and 7017 Al-alloy at R=0.5 in salt solution.

Conclusions

From the study above, the following conclusions can be drawn:

1.The influence of salt solution was significant at low stress ratios in relation to the FCGR behavior of AMC225 MMC and the unreinforced alloy. However, the effect of the salt environment on FCGR diminished as the stress ratio increased.

2.Increasing the stress ratio significantly enhanced the FCGR in both the composite and the base alloy. The salt solution enhanced the FCGR compared to the crack growth response in air at all stress ratio levels.

3.The AMC 225 composite showed superior crack growth resistance at low stress ratio R=0.1. This was attributed to roughness-induced crack closure and crack deflection around fine SiC particles.

However, the beneficial effects of reinforcement disappeared at high R=0.5 ratio due to the absence of crack closure and reduced crack deflection compared to the base alloy.

Acknowledgement: The Author thanks Prof. Dr. W. J. Evans and Prof. Dr. Martin Bache at the University of Wales, Swansea for their great assistance and help. The work described here was carried out in the Department of Materials Engineering at University of Wales, Swansea.

References

Bache, M.R., Evans, W.J., Shakesheff, A., J., Shields, J., Uygur, (2000). I., Influence of aqueous salt environments on fatigue response of SiCp reinforced aluminium alloys. *Materials Science and Technology,* 16 (2) 825-830.

Djukic M.B., Bakic, G.M., Sijacki Zeravcic V., Sedmak A., Rajicic B. (2019). The synergistic action and interplay of hydrogen embrittlement mechanisms in steels and iron: localized plasticity and decohesion. *Engineering Fracture Mechanics*, 216, 106528.

Lee, H.W., Djukic, M.B, Basaran, C., (2023). Modelling fatigue life and hydrogen embrittlement of BCC steel with unified mechanics theory. *International Journal of Hydrogen Energy*, 48(54), 20773-20803

Lu, Z.J., (1999). Environmentally assisted small crack propagation in an Al-Zn-Mg alloy. *PhD Thesis*, University of Wales, SWANSEA, U.K.

Mizoguchi, T., Koyama, M., Noguchi, H., (2018). Qualification method for parameters affecting multi-scale roughness-induced fatigue crack closure. *Procedia Structural Integrity*, 13, 1071–1075

Uygur, I. (1999). Environmentally assisted fatigue response of Al-Cu-Mg-Mn with SiC particulate metal matrix composites, *PhD Thesis*, University of Wales, SWANSEA, U.K.

Uygur, I., Kulekci, M.K., (2002). Low cycle fatigue properties of 2124/SiCp Al-alloy composites. *Turkish Journal of Engineering & Environmental Sciences*, 26 (3) 265-274

Uygur, I., (2004). Tensile Behaviour of Powder Metallurgy Processed (AI-Cu-Mg-Mn)/SiCp Composites. *Iranian Journal of Science & Technology*, B28 (B2), 239-248.

Uygur, I., Evans, W.J., Bache, M., Gulenc, B., (2004). The fatigue behaviour of SiC particulate reinforced 2124 Aluminium

matrix composites. *Metallofizika Noveishie Technologii,* 26 (7) 927-939

Uygur, I., (2011). Notch Behavior and Fatigue Life Predictions of Discontinuously Reinforced MMCs. *Archives of Metallurgy and Materials,* 56 (1) 109-115

Uygur, I., Cicek, A., Toklu, E., Kara, R., Saridemir, S., (2014). Fatigue life predictions of metal matrix composites using artificial neural networks. *Archives Metallurgy and Materials*, 59 (1) 97-103.

Uygur, I., (2024). Influence of particle sizes and volume fractions on fatigue crack growth rates of aerospace Al-alloys composites. *Archives of Metallurgy and Materials*, 1, (Article in press)

CHAPTER V

Graphene/Graphene-Based Transparent Conductive Electrodes

Necmi Serkan TEZEL[1]
Fatma MEYDANERİ TEZEL[2]

Introduction

Depletion of fossil fuel sources, urgent environmental problems and global warming, incremental energy consumption and the humanitarian belief in energy-based applications, clean renewable and sustainable energy mechanism have turned into an progressively substantial problem (Yang et al., 2016). In this contexture, solar cells (Van Franeker et al., 2015; Yang et al., 2015; Nie et al., 2015), lithium batteries (Liang et al., 2015; Zhao et al., 2014) and

[1] Prof. Dr., Karabük University, Faculty of Engineering, Department of Electric-Electronic Engineering, Karabük, Türkiye, ORCID No: 0000-0002-9452-677X, E-mail:nstezel@karabuk.edu.tr
[2] Prof. Dr., Karabük University, Faculty of Engineering, Department of Metallurgy and Materials Engineering, 78050, Karabük, Türkiye.E-mail: fatmameydaneri@karabuk.edu.tr, ORCID: 0000-0003-1546-875X

supercapacitors (Simon& Gogotsi, 2008; Kou et al., 2014) attract much attention from academic and industrial perspectives.

The intense interest in graphene has focused above all on its excellent properties and unique 2D crystal lattice, which offer unique possibilities that address residual global energy demands. The design of graphene-based composites (such as transition metals, metal oxides and conductive polymers) containing a large proportion of active structures by in situ hybridization and ex situ recombination can be evaluated with their microstructure and hybrid architecture (Yang et al., 2016).

Over the past decade, nanocarbons, metal-involving compounds, and functional nanocomposites with curious nanoscopic structure-addicted features have been improved on a large scale. These ingredients are promising for basic investigation and advancements in energy alternation and storage executions (Yu et al., 2013; Sun et al., 2012; Guo et al., 2008). But, such technics must provide the demand for productivity distinctives that include high power rating and energy storage, adoptable productivity-price incidence, long cycleability, operating safety, and wide conversion efficiency. Such materials must overcome such challenges, with executions in devourer electronics, portative instruments, electric transports, hybrid electric transports, and power systems as well as in military and industrial technology. Obviously, the search for improver nanomaterials with desired functions and targeted nanostructures for sophisticated energy executions is a requirement and conspicuous research area (Yang et al., 2016).

Effective method providing controlled deposition and uniform form of rGO thin films over wide-surface, large-scale growth of graphene films for stretchable transparent electrodes, use of graphene-based conductive thin films and GO-based mostly photonic and optoelectronic appliances and equipment (inorganic, organic and window electrodes of dye-sensitized solar cells, organic LEDs, LE electrochemical cells, touch displays, flexile smart windows, graphene-based saturated absorbers in laser cavities for

ultrafast issue, transparent heaters for automobile glass defogging and de-icing, heated smart windows, high- productivity OFETs, flexible and transparent acoustical actuators and nanogenerators, etc.) (Nguyen&Nguyen, 2016) is promising applications and researchs for graphene-based transparent and flexible conductive films.

Graphene′ structure and properties

Graphene has a 2D crystal structure with a hexagonal honeycomb lattice structure and sp^2 hybridization of C atoms (Fig.1a). The thickness of the monolayer graphene is 0.35 nm and the C-C bond length is 0.142 nm. There are 3 electrons in the outermost shell of C atoms, which are formed by influential σ bonds during sp^2 hybridisation, and the 4th electrons are connected as π bonds. Fig. 1(b) depicts the Brillouin zone of graphene in the unit cell.

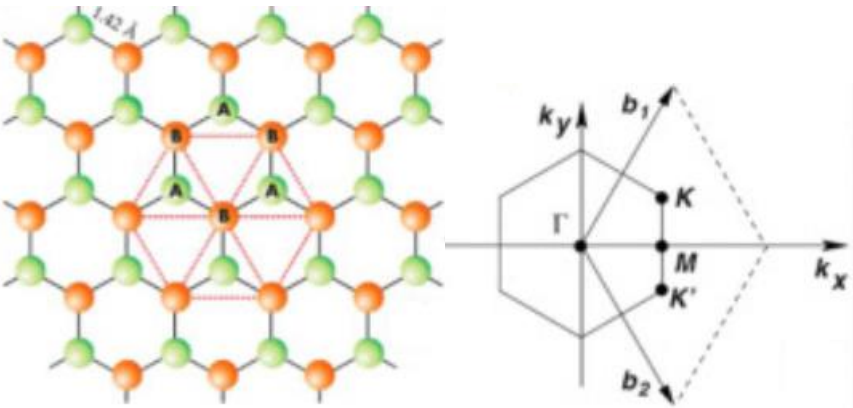

a) *b)*

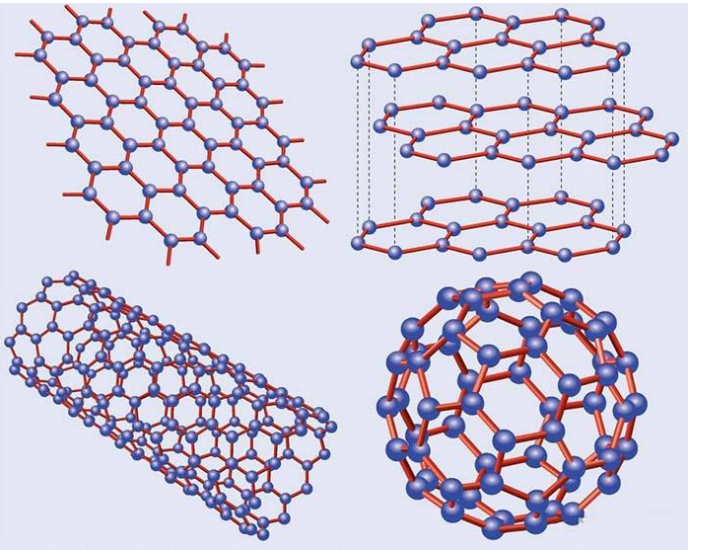

c)

Fig.1. a) 2D graphene structure b) Brillouin zone of graphene c) Carbon nanomaterials with graphene (Wang et al., 2019).

The steady hexagonal plane system executes graphene flexible and resolute. Graphene, as the fundamental unit of most carbon nanomaterials, can be stacked into graphite and OD fullerenes and folded into carbon nanotube (Fig.1c) (Wang et al., 2019). This incomparable crystal system and innovative electronic chemistry of graphene is the reason for many of its mechanics, thermic, optics and electrical qualifications. The conduction and valence straps, which indicate the two sublattices of A and B in the unit cell, connect them to the K points at the border of the first Brillouin zone, which is a zero band structure (Fig.2) (Wang et al., 2019; Lee et al., 2008; Balandin et al., 2008; Bolotin et al., 2008; Neto et al., 2009).

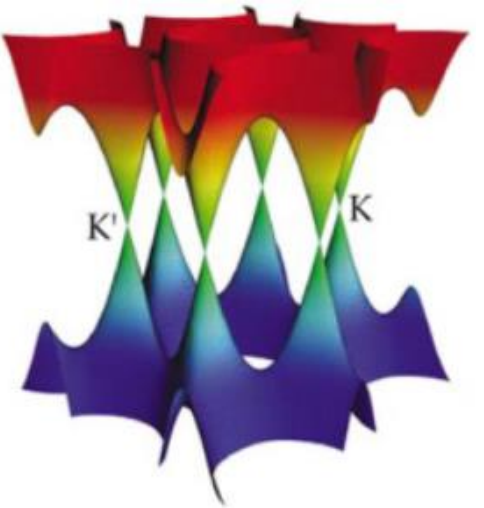

Fig.2. At K and K' points of graphene, the conduction band touches to the valence band (Wang et al., 2019; Lee et al., 2008; Balandin et al., 2008; Bolotin et al., 2008; Neto et al., 2009).

The graphene′ thermal conductivity of is about 5000 W mK^{-1} at room temperature. Moreover, the graphene′ μ_e of at room temperature is as precipitous as 1.5×10^4 cm^2 V^{-1} s^{-1} (Wang et al., 2019). It has very good mechanical strength up to approximately 1 TPa. Graphene-based nanomaterials with their superior electrical conductibility and superior specific surface region (2630 $m^2.g^{-1}$), along with properties such as chemical resolution, thermic resolution, and mechanics flexibility, have been commonly investigated to be electrode materials for flexible electrochemical supercapacitor devices (FESDs) (Bonaccorso et al., 2015; Low et al., 2016). This superior chemical resolution and electrochemical service also enables it to be a catalyst promote for fuel cells or an active metal-free electrocatalyst (Kong et al., 2014; Liu et al., 2014). Graphene also has other electric particulars such as abnormal quantum hall effects (QHEs), ambipolar electric field effects, Klein tunneling and ballistic conduction (Wang et al., 2019). In addition to the features of graphene explained above, it is a very expecting ingredients that will replace with the expensive and brittle ITO as

pellucid electrodes for further optoelectronics and photovoltaics (Han et al., 2012; Bonaccorso et al., 2010). This single-layer carbon is appropriate for the development of energy transformation and deposition.

Graphene, as an ordinary 2D nanometer-scale ingredient, has extraordinary optoelectronic features owing to its distinctive band fabric. Besides, these actual optoelectronic features, the hybridisation and heterostructure of graphene with other 2D ingredients and the modify in the form and mode of graphene allow graphene-based hybridized materials and heterostructures with unique photoelectric properties (Wang et al., 2019). Layer-to-layer Vander Waals interplays can cause to restacking of graphene plates (GPs), which is a trouble in implementation processes. Normally, the operative specific surface area of graphene concerned to the count of graphene sheets may decrease significantly, thus leading to rapid decrease in the conduction of ions during charge/discharge. To intercept the re-stacking of graphene sheets, arched and wrinkled graphene structures are developed with the accidences of 1D, 2D and 3D graphene fibers, films and foams, respectively. Furthermore, regarding its 2D structural features, graphene can form an ideal structure for controlled operationalization with other electro-effective constituents such as metal oxides and conductive polymers, and consequently graphene-based hybrid nanostructures present admirable features for FESDs with superior power and energy intensity (Song&Zeng, 2015).

Outside of its electrochemical performance, the flexibility distinctives of graphene ingredients are of perfect significance. Accordingly structural definitions, nanostructured graphene ingredients can be categorized as graphene nanoribbons, microspheres, balls, nanoscrolls, representing 1D, 2D and 3D graphene fibers, films and foams, respectively. Amongst them, 1D fibers are combined with 2D microscopic rGO layers lined up the direction of the fiber axis; 2D films are constructed by sequential arrangement of rGO layers and 3D foams are generally constructed

with a porous structure with fine mechanics strength as a outcome of the fine flexible of FESDs (Guo et al., 2017).

Graphene′ synthesis methods

Properties of graphene, such as the amount of layers, morphology and structure, imperfectness and impureness substances, dissolubility, collateral dimension and superficial chemistry, appertain entirely on the synthetical methods applicated. The syntheses of graphene involves diverse methods, mainly top-down and bottom-up, and is given in Fig.3. The most commonly used methods among these are mechanics exfoliation, reduction of graphene oxide, chemical vapor deposition (CVD) and epitaxial growth (Fig.4)(Hossain et al., 2010).

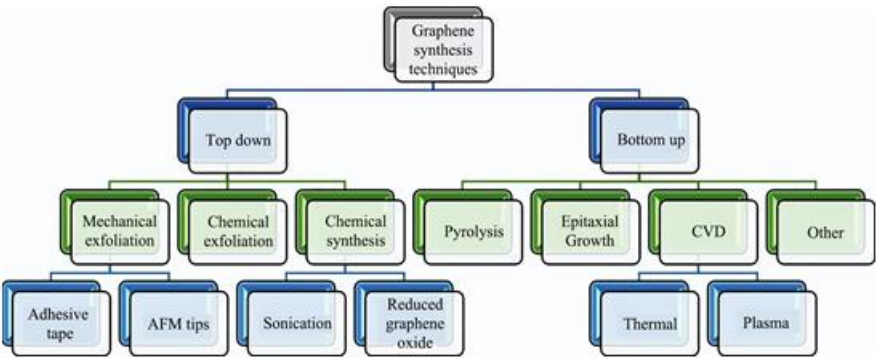

Fig. 3. Graphene Synthesis methods (Hossain et al., 2010).

Mechanics exfoliation

Micromechanics or solid-phase exfoliation

Mechanics exfoliation is a top-down technique that is shaped transversely and longitudinally on the layered surface. The sheets of graphene are kept jointly by ineffectual van der Waals actions to create graphite, with the energy and interval of the intermediate connection being 2eV/nm^2 and 3.34 Å, seriatim, and an exterior force of approximately ~300 nN/μm^2 is required to remove one layer of graphite (Zhang et al., 2005). The micromechanics process is easy

and does not need particular fittings. An amount tape is added onto the facet of the graphite and after that sealed. Graphite sheets adhered to this adhesive split along the crystal plane. This approach is to obtain monolayer graphene sheets with a thickness of approximately 0.4 nm and down to microns of the collateral dimension (Yang et al., 2016). Though the procedure is easy, it is not conducive to the production of superior grade specimens in terms of charge activity, refinement, imperfections and optelectronic features.

Liquid-phase exfoliation

Exfoliation of graphite within its individualistic sheets is strong even so ineffectual van der Waals actions between neighboring sheets. Therefore, for prospering exfoliation, van der Waals actions between neighboring sheets involve to dominate. Liquid immersion, in reducing the liquid medium relative to vacuum, distributive London interplays subscribe to the potential energy between neighboring sheets, which is one of the most current attitudes to decreasing van der Waals actions (Monajjemi, 2017). The high tension at the solid and liquid interface is a result of the poor solubility of the strict in the fluid (Israelachvili, 2011). Therefore, it is very important to choose superior superficial strain liquids to discrete graphitic sheets and graphene. Because these liquids decrease the interfacial strain between graphene and liquid. In fact, when the surfactants are used for especially surfactants with high adsorption energy on graphene, much higher than the liquid molecule, the exfoliation of graphene from graphite can be improved and graphene can interact. Additionally, added surfactants stabilize exfoliated graphene in inorganic solution.

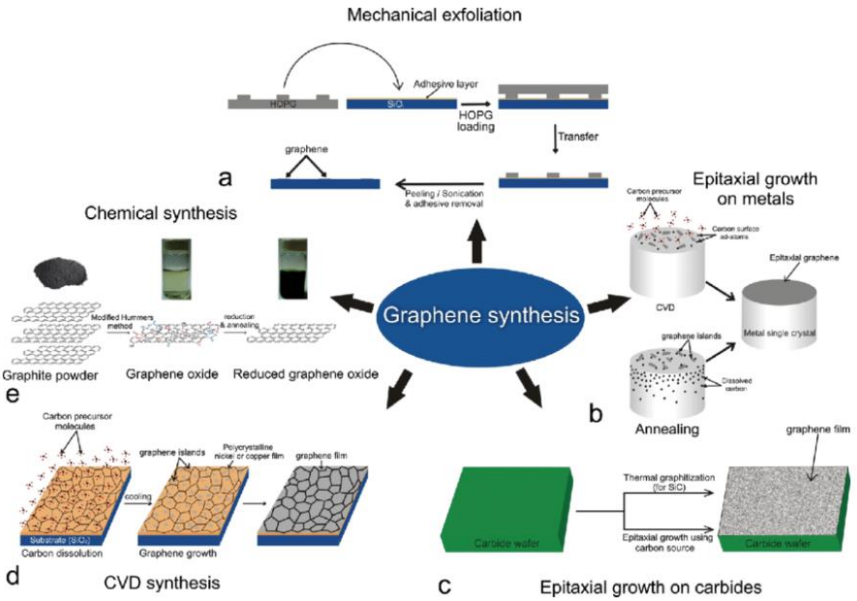

Fig.4. Synthesis methods of graphene a) Mechanical exfoliation, b,c) Epitaxial growth of graphene, d)CVD method, e) chemical synthesis (Gao et al., 2009).

Reduction of graphene oxide

Alternative process of producing graphene is the reduction of GO and is the top-down procedure. First the fabric of graphene, graphene oxide must be produced from graphite. There are diverse attitudes to producing graphene oxide, such as Brodie synthesis, Staudenmaier rocess and Staudenmaier-Hoffman-Hamdi process, only the most suitable process is Hummers' procedure (Hummers Jr& Offeman, 1958). Here, graphene oxide (GO) is synthesized by mixing graphite sodium nitrate, sulfuric acid and potassium permanganate. The prepared GO is synthesized in the subsequent stage by different procedures containing thermal reduction (Liu et al., 2013), solvothermal reduction (Yuan et al., 2014), hydrothermal reduction (Zheng et al., 2017) and chemical reduction (Chua& Pumera, 2014).

Graphene′ epitaxial growth

The graphene′ epitaxial growth is achieved by thermic resolution of the SiC substratum (Yu et al., 2011). It can be developed on 0001 (silicon-end) and $000\bar{1}$ (carbon-end) surfaces of 4H-SiC and 6H-SiC. Sublimation of Si from SiC substratum begins to occur when these substratums are heated to approximately 1300°C (De Heer et al., 2007), usually under ultra-high vacuum circumstance to avoid impurities (Yu et al., 2011). Emtsev and colleagues (Emtsev et al., 2009) conducted experiments at much higher Ar atmospheric pressure at wide range heating temperatures and observed that the presence of Argon significantly improved the surface morphology. This is because it prevents the eliminatin of Si atoms from SiC and reduces the sublimation ratio (Emtsev et al., 2009). Growing onto the SiC 0001 surface is leisurely, and very thin specimens, down to monolayers, can be produced in relatively short times and at high temperatures (Berger et al., 2006). In addition, there are also epitaxial graphene production approaches for growth on SiC substrate, which include the departure of carbon atoms from metal substratums and the dissociation of hydrocarbon gas on other carbide substratums (Singh et al., 2011).

Chemical vapour deposition (CVD)

CVD is one of the most suitable methods for fabricating superior-qualification graphene on a great- scale (Esfandiar et al., 2011). CVD processes involve raising such gases (such as H_2 and Ar) into a reactor and leading them towards a hot region where decompose of hydrocarbon precursors on a metal substratum to form monolayers and multilayers of graphene. The purpose of this metal substrate is to act as a catalyst by reducing the energy supposed for dissociation, along certain mechanisms of graphene storage, which properly affects the qualification of graphene (Zhang et al., 2013). Therefore, procedure parameters such as catalysts, gas flux ratio, precursors, pressure, time and temperature are very significant in assigning the qualification of graphene.

Electrode applications

Transparent conductive electrodes (TCEs) are an important component of optoelectronic apparatus. Nowadays, n-type semiconductor ITO-based TCEs are utilized in PSCs and have a suitable work function (4.2–5.3 eV), more than 80% transmittance at 550 nm, and Rs=5–400 Ω/sq per unit area based on industrial standards (Gordon, 2000). However, ITO faces serious problems such as instability in acidic and basic environments, inherent brittleness, limited indium reserves and high production costs (Wan et al., 2011). Graphene transparent films with superior conductivity, transparency, perfect charge activity, mechanics flexible and nominal expense can be reflected as some of the most expectation TCE materials to replace ITO (Wan et al., 2012; Wan et al., 2011; Pang et al., 2011).

Generally, the T values of graphene films are invertedly rational to their thickness. For instance, thermic polymerization of superphenalene derivatives can fabricate graphene films with thicknesses of 30, 22, 12, and 4 nm, indicating a transmittance of 55, 66, 80, and 90%, respectively, in the visible region (500 nm) (Wang et al., 2008). For micromechanics exfoliated and CVD-grown graphene films, these T values decrease linearly with improving count of layers. For example, graphene thin films produced by CVD with 1, 2, 3, and 4 sheets show a transmittance of 97.4, 95.1, 92.9, and 90.1% at 500 nm, respectively (Bae et al., 2010). Nevertheless, when aromatic molecules and GO-derived graphene films are compared with exfoliated and CVD-produced graphene films, graphene shows over T values for the identical number of layers, indicating that film thicknesses are suitable for light transmittance owing to the asset of topological imperfections (Wang et al., 2008; Gómez-Navarro et al., 2010). Also, graphene′ thicker films have superior electron conductivity and lower Rs value. Li et al. (Li et al., 2008) produced graphene films by depositing liquid-exfoliated graphene layers on quartz layer by layer, and 1, 2 and 3 layer LB films had values of approximately 150, 20 and 8 kΩ and up to transmittance of 93, 88, and 83% at 1000 nm, respectively. The

electron conductivity′ strengthening enhances the achievement of low Rs for TCE, so the ideal equilibriate among T and Rs is need to graphene films (Yang et al., 2016).

The relationship between T and Rs can be controlled by the ratio σ_{dc}/σ_{op} and is fundamental for TCEs (De et al., 2010). Moreover, T, Rs and σ_{dc}/σ_{op} of graphene films strongly depend on the crystal and film qualification, which are nearly concerned to both the graphene source and production procedures. For commercial purposes T≥90%, Rs≤100 Ω/sq and $\sigma_{dc}/\sigma_{op} \geq 35$ TCE are recommended. De and Coleman (De&Coleman, 2010) proposed substrate-supported additives into graphene with potentials of T ≈ 91% and Rs = 11 Ω/sq, σ_{dc}/σ_{op} up to 330, which are much more adequate for industrial applications of TCE. Experimentally, Blake et al. (Blake et al., 2008) described the utilize of a sheet of PVA to cause the generation of micromechanics-exfoliated graphene with n-type doping, with $\mu \approx 3 \times 10^{12}$ cm^{-2}, T ≈ 98% and Rs = 400 Ω/sq. These outcomes obviously depict that graphene-derived TCEs, with doping-combination, are potentially better than ITO in solar cell implementations.

CVD-produced graphene thin films with much better qualification and superior electric conductivity confronted to both rGO and chemically fabricated graphene films generally exhibit large PCEs, allowing applications of TCE-based PSCs. Nevertheless, CVD growth of multicomponent layered ingredients is much less desirable for apparatus applications and requires quite frequent transfers. TCEs derived from rGO films can be readily deposited onto desired substratums by applying solution processes that are low cost, reproducible, and with high efficiency (Geng et al., 2010; Park et al., 2014). High conductivity films from this rGO are difficult to produce on a large scale. But the current results may provide a completely basic requirement for some optoelectronic apparatus such as touch and flat panel displays and LEDs. Note that a TCE is only one part in a PSC. The project, production and combining of operative apparatus play a fundamental role for superior output. Nevertheless, there is still potential for perfecting the qualification of graphene and its thin films (Skaltsas et al., 2012;

Guardia et al., 2011), enhancing its performance, optimizing (both active sheet and conduction sheet materials) and manufacturing processes of apparatus (Buzaglo et al., 2013; Seo et al., 2011).

Unlike the photoanode, optical transparency is not a prerequisite for the catalytic counter electrode. In most cases GCEs are impermeable to visible light. However, it also has some benefits; optically transparent counter electrodes include particular applied implementations in windows, roof panels and decorative applications, from the production of plastic DSSCs to the integration of photovoltaic systems such as tandem DSSCs (Secor et al., 2013; Ahn et al., 2007).

Conclusion

In this study, information is given about the structure of graphene and its production methods for graphene-based transparent and flexible conductive electrodes. The decrease in indium reserves and the expensiveness of the ITO substrate have led scientists towards graphene-based thin films. Among the top-down and bottom-up production methods, information is given about the advantages and disadvantages of the most commonly used methods, their efficiency depending on the number of layers, and the reasons affecting the quality of the films. Although the CVD method is successful in large-scale coatings, it is a disadvantage that it requires continuous transfer in multi-component systems. Transparent flexible conductive electrode structures that can be used for dye-sensitized solar cells, polymer supercapacitors, touch screens, flat panel displays, and most optoelectronic and photovoltaic components are still being developed.

References

Ahn, K. S., Yoo, S. J., Kang, M. S., Lee, J. W., & Sung, Y. E. (2007). Tandem dye-sensitized solar cell-powered electrochromic devices for the photovoltaic-powered smart window. Journal of Power Sources, 168(2), 533-536.

Bae, S., Kim, H., Lee, Y., Xu, X., Park, J. S., Zheng, Y., ... & Song, Y. I. (2010). Roll-to-roll production of-inch graphene lms for transparent electrodes. Nature nanotechnology,5, p.574

Balandin, A. A., Ghosh, S., Bao, W., Calizo, I., Teweldebrhan, D., Miao, F., & Lau, C. N. (2008). Superior thermal conductivity of single-layer graphene. Nano letters, 8(3), 902-907.

Berger, C., Song, Z., Li, X., Wu, X., Brown, N., Naud, C., ... & de Heer, W. A. (2006). Electronic confinement and coherence in patterned epitaxial graphene. Science, 312(5777), 1191-1196.

Blake, P., Brimicombe, P. D., Nair, R. R., Booth, T. J., Jiang, D., Schedin, F., ... & Novoselov, K. S. (2008). Graphene-based liquid crystal device. Nano letters, 8(6), 1704-1708.

Bolotin, K. I., Sikes, K. J., Jiang, Z., Klima, M., Fudenberg, G., Hone, J., ... & Stormer, H. L. (2008). Ultrahigh electron mobility in suspended graphene. Solid state communications, 146(9-10), 351-355.

Bonaccorso, F., Sun, Z., Hasan, T., & Ferrari, A. C. (2010). Graphene photonics and optoelectronics. Nature photonics, 4(9), 611-622.

Bonaccorso, F., Colombo, L., Yu, G., Stoller, M., Tozzini, V., Ferrari, A. C., ... & Pellegrini, V. (2015). Graphene, related two-dimensional crystals, and hybrid systems for energy conversion and storage. Science, 347(6217), 1246501.

Buzaglo, M., Shtein, M., Kober, S., Lovrinčić, R., Vilan, A., & Regev, O. (2013). Critical parameters in exfoliating graphite into

graphene. Physical Chemistry Chemical Physics, 15(12), 4428-4435.

Chua, C. K., & Pumera, M. (2014). Chemical reduction of graphene oxide: a synthetic chemistry viewpoint. Chemical Society Reviews, 43(1), 291-312.

De Heer, W. A., Berger, C., Wu, X., First, P. N., Conrad, E. H., Li, X., ... & Martinez, G. (2007). Epitaxial graphene. Solid State Communications, 143(1-2), 92-100.

De, S., King, P. J., Lyons, P. E., Khan, U., & Coleman, J. N. (2010). Size effects and the problem with percolation in nanostructured transparent conductors. ACS nano, 4(12), 7064-7072.

De, S., & Coleman, J. N. (2010). Are there fundamental limitations on the sheet resistance and transmittance of thin graphene films?. ACS nano, 4(5), 2713-2720.

Emtsev, K. V., Bostwick, A., Horn, K., Jobst, J., Kellogg, G. L., Ley, L., ... & Seyller, T. (2009). Towards wafer-size graphene layers by atmospheric pressure graphitization of silicon carbide. Nature materials, 8(3), 203-207.

Esfandiar, A., Akhavan, O., & Irajizad, A. (2011). Melatonin as a powerful bio-antioxidant for reduction of graphene oxide. Journal of Materials Chemistry, 21(29), 10907-10914.

Gao, W., Alemany, L. B., Ci, L., & Ajayan, P. M. (2009). New insights into the structure and reduction of graphite oxide. Nature chemistry, 1(5), 403-408.

Geng, J., Kong, B. S., Yang, S. B., & Jung, H. T. (2010). Preparation of graphene relying on porphyrin exfoliation of graphite. Chemical Communications, 46(28), 5091-5093.

Gómez-Navarro, C., Meyer, J. C., Sundaram, R. S., Chuvilin, A., Kurasch, S., Burghard, M., ... & Kaiser, U. (2010). Atomic structure of reduced graphene oxide. Nano letters, 10(4), 1144-1148.

Gordon, R. G. (2000). Criteria for choosing transparent conductors. MRS bulletin, 25(8), 52-57.

Guardia, L., Fernández-Merino, M. J., Paredes, J. I., Solís-Fernández, P., Villar-Rodil, S., Martínez-Alonso, A., & Tascón, J. M. D. (2011). High-throughput production of pristine graphene in an aqueous dispersion assisted by non-ionic surfactants. Carbon, 49(5), 1653-1662.

Guo, X., Zheng, S., Zhang, G., Xiao, X., Li, X., Xu, Y., ... & Pang, H. (2017). Nanostructured graphene-based materials for flexible energy storage. Energy Storage Materials, 9, 150-169.

Guo, Y. G., Hu, J. S., & Wan, L. J. (2008). Nanostructured materials for electrochemical energy conversion and storage devices. Advanced Materials, 20(15), 2878-2887.

Han, T. H., Lee, Y., Choi, M. R., Woo, S. H., Bae, S. H., Hong, B. H., ... & Lee, T. W. (2012). Extremely efficient flexible organic light-emitting diodes with modified graphene anode. Nature photonics, 6(2), 105-110.

Hossain, S., Abdalla, A. M., Suhaili, S. B., Kamal, I., Shaikh, S. P., Dawood, M. K., & Azad, A. K. (2020). Nanostructured graphene materials utilization in fuel cells and batteries: A review. Journal of Energy Storage, 29, 101386.

Hummers Jr, W. S., & Offeman, R. E. (1958). Preparation of graphitic oxide. Journal of the american chemical society, 80(6), 1339-1339.

Israelachvili, J. N. (2011). Electrostatic forces between surfaces in liquids. Intermolecular and surface forces, 291-340.

Kong, X. K., Chen, C. L., & Chen, Q. W. (2014). Doped graphene for metal-free catalysis. Chemical Society Reviews, 43(8), 2841-2857.

Kou, L., Huang, T., Zheng, B., Han, Y., Zhao, X., Gopalsamy, K., ... & Gao, C. (2014). Coaxial wet-spun yarn supercapacitors for

high-energy density and safe wearable electronics. Nature communications, 5(1), 3754.

Lee, C., Wei, X., Kysar, J. W., & Hone, J. (2008). Measurement of the elastic properties and intrinsic strength of monolayer graphene. science, 321(5887), 385-388.

Li, X. L., ZhangGY, B. X., SunXM, W., & Wang, E. andDaiH J (2008). Highly conducting graphene sheets and Langmuir-Blodgett filmsNat. Nanotechnol, 3, 538-42.

Liang, X., Hart, C., Pang, Q., Garsuch, A., Weiss, T., & Nazar, L. F. (2015). A highly efficient polysulfide mediator for lithium–sulfur batteries. Nature communications, 6(1), 5682.

Liu, X., Kim, H., & Guo, L. J. (2013). Optimization of thermally reduced graphene oxide for an efficient hole transport layer in polymer solar cells. Organic Electronics, 14(2), 591-598.

Liu, M., Zhang, R., & Chen, W. (2014). Graphene-supported nanoelectrocatalysts for fuel cells: synthesis, properties, and applications. Chemical reviews, 114(10), 5117-5160.

Low, J., Cheng, B., Yu, J., & Jaroniec, M. (2016). Carbon-based two-dimensional layered materials for photocatalytic CO_2 reduction to solar fuels. Energy Storage Materials, 3, 24-35.

Monajjemi, M. (2017). Liquid-phase exfoliation (LPE) of graphite towards graphene: An ab initio study. Journal of Molecular Liquids, 230, 461-472.

Neto, A. C., Guinea, F., Peres, N. M., Novoselov, K. S., & Geim, A. K. (2009). The electronic properties of graphene. Reviews of modern physics, 81(1), 109.

Nguyen, B. H., & Nguyen, V. H. (2016). Promising applications of graphene and graphene-based nanostructures. Advances in Natural Sciences: Nanoscience and Nanotechnology, 7(2), 023002.

Nie, W., Tsai, H., Asadpour, R., Blancon, J. C., Neukirch, A. J., Gupta, G., ... & Mohite, A. D. (2015). High-efficiency solution-processed perovskite solar cells with millimeter-scale grains. Science, 347(6221), 522-525.

Pang, S., Hernandez, Y., Feng, X., & Müllen, K. (2011). Graphene as transparent electrode material for organic electronics. Advanced Materials, 23(25), 2779-2795.

Park, J. S., Yu, L., Lee, C. S., Shin, K., & Han, J. H. (2014). Liquid-phase exfoliation of expanded graphites into graphene nanoplatelets using amphiphilic organic molecules. Journal of colloid and interface science, 417, 379-384.

Secor, E. B., Prabhumirashi, P. L., Puntambekar, K., Geier, M. L., & Hersam, M. C. (2013). Inkjet printing of high conductivity, flexible graphene patterns. The journal of physical chemistry letters, 4(8), 1347-1351.

Seo, J. W. T., Green, A. A., Antaris, A. L., & Hersam, M. C. (2011). High-concentration aqueous dispersions of graphene using nonionic, biocompatible block copolymers. The Journal of Physical Chemistry Letters, 2(9), 1004-1008.

Simon, P., & Gogotsi, Y. (2008). Materials for electrochemical capacitors. Nature materials, 7(11), 845-854.

Singh, V., Joung, D., Zhai, L., Das, S., Khondaker, S. I., & Seal, S. (2011). Graphene based materials: past, present and future. Progress in materials science, 56(8), 1178-1271.

Skaltsas, T., Karousis, N., Yan, H. J., Wang, C. R., Pispas, S., & Tagmatarchis, N. (2012). Graphene exfoliation in organic solvents and switching solubility in aqueous media with the aid of amphiphilic block copolymers. Journal of Materials Chemistry, 22(40), 21507-21512.

Song, J., & Zeng, H. (2015). Transparent electrodes printed with nanocrystal inks for flexible smart devices. Angewandte Chemie International Edition, 54(34), 9760-9774.

Sun, Y. K., Chen, Z., Noh, H. J., Lee, D. J., Jung, H. G., Ren, Y., ... & Amine, K. (2012). Nanostructured high-energy cathode materials for advanced lithium batteries. Nature materials, 11(11), 942-947.

Van Franeker, J. J., Turbiez, M., Li, W., Wienk, M. M., & Janssen, R. A. (2015). A real-time study of the benefits of co-solvents in polymer solar cell processing. Nature communications, 6(1), 6229.

Wan, X., Long, G., Huang, L., & Chen, Y. (2011). Graphene–a promising material for organic photovoltaic cells. Advanced Materials, 23(45), 5342-5358.

Wan, X., Huang, Y., & Chen, Y. (2012). Focusing on energy and optoelectronic applications: a journey for graphene and graphene oxide at large scale. Accounts of chemical research, 45(4), 598-607.

Wang, J., Mu, X., Sun, M., & Mu, T. (2019). Optoelectronic properties and applications of graphene-based hybrid nanomaterials and van der Waals heterostructures. Applied Materials Today, 16, 1-20.

Wang, X., Zhi, L., Tsao, N., Tomović, Ž., Li, J., & Müllen, K. (2008). Transparent carbon films as electrodes in organic solar cells. Angewandte Chemie International Edition, 47(16), 2990-2992.

Yang, Y., Han, C., Jiang, B., Iocozzia, J., He, C., Shi, D., ... & Lin, Z. (2016). Graphene-based materials with tailored nanostructures for energy conversion and storage. Materials Science and Engineering: R: Reports, 102, 1-72.

Yang, Y., Chen, W., Dou, L., Chang, W. H., Duan, H. S., Bob, B., ... & Yang, Y. (2015). High-performance multiple-donor bulk heterojunction solar cells. Nature photonics, 9(3), 190-198.

Yu, G., Xie, X., Pan, L., Bao, Z., & Cui, Y. (2013). Hybrid nanostructured materials for high-performance electrochemical capacitors. Nano Energy, 2(2), 213-234.

Yuan, B., Bao, C., Qian, X., Wen, P., Xing, W., Song, L., & Hu, Y. (2014). A facile approach to prepare graphene via solvothermal reduction of graphite oxide. Materials Research Bulletin, 55, 48-52.

Yu, X. Z., Hwang, C. G., Jozwiak, C. M., Köhl, A., Schmid, A. K., & Lanzara, A. (2011). New synthesis method for the growth of epitaxial graphene. Journal of Electron Spectroscopy and Related Phenomena, 184(3-6), 100-106.

Zhang, Y., Small, J. P., Pontius, W. V., & Kim, P. (2005). Fabrication and electric-field-dependent transport measurements of mesoscopic graphite devices. Applied Physics Letters, 86(7).

Zhang, Y. I., Zhang, L., & Zhou, C. (2013). Review of chemical vapor deposition of graphene and related applications. Accounts of chemical research, 46(10), 2329-2339.

Zhao, M. Q., Zhang, Q., Huang, J. Q., Tian, G. L., Nie, J. Q., Peng, H. J., & Wei, F. (2014). Unstacked double-layer templated graphene for high-rate lithium–sulphur batteries. Nature communications, 5(1), 3410.

Zheng, X., Peng, Y., Yang, Y., Chen, J., Tian, H., Cui, X., & Zheng, W. (2017). Hydrothermal reduction of graphene oxide; effect on surface-enhanced Raman scattering. Journal of Raman spectroscopy, 48(1), 97-103.


BIDGE